AN ABSTRACT OF THE DISSERTATION OF

Benjamin T. Dickinson for the degree of Doctor of Philosophy in Mechanical
Engineering presented on August 12, 2009.

Title: Detecting Fluid Flows with Bioinspired Hair Sensors

Abstract approved:

_____

Belinda A. Batten

Many animals detect prey or enhance their locomotion with information
from hair-like receptors that are activated by local fluid flows. The util-
ity of biological hair receptors has motivated the design of artificial hair
sensors (AHS) for flow control applications where aerodynamic or hydro-
dynamic forces play a significant role in the dynamics of a body. Among
the potential applications for AHS are low-Reynolds number flyers for
enhanced maneuverability and underwater vehicles for greater efficiency
while navigating. For such applications, how flow phenomena related to
aerodynamically or hydrodynamically important forces can be detected
through the mechanical response of AHS must be understood. In this
collection of manuscripts, we investigate the utility of AHS for detecting
flow phenomena pertinent to these applications.

One aerodynamically adverse phenomena of low-Reynolds number flight is boundary layer separation. By modeling each hair as a viscoelastic beam coupled to its local flow environment, the dynamic and mechanical response of a hair sensor array was simulated in unsteady flow separation. We show that the resultant moment at the base of each hair sensor in the array provides a space and time accurate representation of the onset and span of reversed flow, the location of the point of zero wall shear-stress, the formation and relative position of near wall vortices, and the spatial development and evolution of boundary layer flows.

The shape of a boundary layer flow is another means of detecting flow separation and is also related to the local wall shear-stress. Here, we determine the hair lengths relative to a general measure of boundary layer thickness that maximizes output sensitivity to changes in boundary layer shape. The range of computed optimal hair lengths is in close agreement with the range of hair receptor lengths measured on three bat species. A tapered hair profile is shown to provide larger sensitivities over a wider range of flow conditions compared to hairs of uniform cross section.

The feedback of surface mounted AHS measurements for accurate flow state estimation away from the wall is important for effective flow control design. A linear quadratic Gaussian observer is designed for an unsteady viscous incompressible flow with hair sensor arrays. Here, the Riccati equation was numerically solved using the modified Kleinman-Newton method combined with a snapshot procedure for solving Lyapunov equations. We show that measurements provided by two patches of hair sensor arrays significantly contributes to the estimation of a nearby region of the flow velocity field.

The results herein support artificial hair sensors as an effective means of detecting flow phenomena important to the dynamics of bodies in fluid flows. Within the following manuscripts, contributions are also made to biology, artificial hair sensor design and application, and linear control theory.

Detecting Fluid Flows with Bioinspired Hair Sensors

by
Benjamin T. Dickinson

A DISSERTATION

submitted to

Oregon State University

in partial fulfillment of
the requirements for the
degree of

Doctor of Philosophy

Presented August 12, 2009
Commencement June 2010

Doctor of Philosophy dissertation of Benjamin T. Dickinson presented on August 12, 2009.

APPROVED:

_____

Major Professor, representing Mechanical Engineering

_____

Head of the School of Mechanical, Industrial, and Manufacturing Engineering

_____

Dean of the Graduate School

I understand that my dissertation will become part of the permanent collection of Oregon State University libraries. My signature below authorizes release of my dissertation to any reader upon request.

_____

Benjamin T. Dickinson, Author

ACKNOWLEDGMENTS

CONTRIBUTION OF AUTHORS

In the first publication, "The Detection of Unsteady Flow Separation with Bioinspired Hair-Cell Sensors," Belinda Batten and John Singler contributed to the initial idea of the experiment ultimately performed therein. John Singler also provided finite element code for Euler-Bernoulli beam simulations. Both Belinda Batten and John Singler provided valuable suggestions throughout the revision process.

The second chapter contains a technical manuscript titled: "Mathematical Modeling of Biologically Inspired Hair Receptor Arrays in Laminar Unsteady Flow Separation." This work was a more in depth and refined version of the conference proceeding cited above. John Singler's name was included based on his contribution to the original idea of the experiments performed. Again, both Belinda Batten and John Singler provided valuable suggestions at each stage of the revision process.

In the fourth chapter, "A Snapshot Algorithm for Linear Feedback Flow Control Design," John Singler provided extensive technical guidance. He also made considerable revisions and contributions to the manuscript during the revision process. These revisions focused on providing adequate mathematical detail and giving the algorithm context within the body of existing control design methodologies. Belinda Batten provided guidance, perspective and feedback on the approach and selection of the problem studied.

TABLE OF CONTENTS

TABLE OF CONTENTS (Continued)

LIST OF FIGURES

LIST OF FIGURES (Continued)

LIST OF FIGURES (Continued)

LIST OF TABLES

Detecting Fluid Flows with Bioinspired Hair Sensors

1   GENERAL INTRODUCTION

The effective use of artificial hair sensors (AHS) for the detection and feedback of information related to aerodynamically or hydrodynamically important fluid flows will require an understanding of the relationships between mechanical quantities of hair-like structures and the particular phenomena or physical quantities specific to the flows of interest. In this collection of manuscripts, we investigate hair-like structures for the detection and feedback of information related to aerodynamically and hydrodynamically important flows. Specifically, we will 1) determine that an AHS array can provide a space and time accurate representation of laminar unsteady flow separation, 2) characterize how hairs physically respond to unsteady viscous incompressible flows and how the mechanical moment and shear force at the base of the hair is related to local flow velocity, 3) determine how hair geometry influences the hair sensitivity in boundary layer flows, 4) develop a tractable mathematical model of hair-like structures for flow control applications, and 5) provide evidence that limited wall measurements from hair sensor arrays can effectively estimate the regions of the flow velocity field through model-based observer design.

Many animals use hair-like structures to detect their flow environments. For example, bats exhibit super-maneuverability in low-Reynolds number regimes of flight and acrobatic-like behavior when landing. While this is likely largely an outcome of the bat's articulated wing structure, bats also possess distributed arrays of hair receptors growing from their wing surfaces. It has been hypothesized that the hair receptor arrays provide instantaneous feedback on the airflow environment over the

wing [1, 2, 3] allowing the bat to adjust its kinematics or wing shape during flight.

Cartilaginous and bony fishes also use mechanosensor arrays of hair-like structures known as the lateral line. By detecting changes in flow environment surrounding the fish, the lateral line has been implicated in prey detection and tracking, collective schooling behavior, and maintaining position and orientation in strong currents [4, 5]. Other examples of biological hair receptors may be found on the legs of crickets [6, 7] and spiders [8, 9].

Inspired by the biological hair receptor, flow feedback provided by AHS is one potential means of detecting aerodynamic or hydrodynamic forces on a body. For example, micro-air-vehicles (MAV) operate in low-Reynolds number flight regimes (Re $\sim 10^5$) with inherent flow unsteadiness and flight stability issues caused by gusts of wind or separation bubbles (see [10] and the references therein). One potential solution to the challenges associated with low-Reynolds number flight is a closed-loop flow control system integrated into the MAV and designed to mitigate the effects of such destabilizing flows. Airflow feedback to controller would be likely provided by measurements of the flow field made from the MAV surface. For this purpose, a suite of surface mounted hair sensor arrays is one potential means of flow detection. However, the successful application of AHS requires an understanding of the relationship between their local flow environment and physical response. This is a general requirement for any AHS application and is addressed here by the 5 research objectives listed above.

The article in Chapter 2 [11] contributes to the first research objective: the mechanical characterization of a hair sensor array in unsteady flow separation. Here, each hair sensor is modeled as a viscoelastic Euler-Bernoulli beam and coupled to the flow with empirical drag coefficients for cylinders in cross-flow. With finite element simulations of the hair-fluid model we found that the moment at the base of the hair

(taken as the hair output signal) provided a time and space accurate representation of the phenomena associated with unsteady flow separation. A linear algebraic hair sensor model was then derived and shown to provide an output similar to the viscoelastic hair simulations.

Chapter 3 [12] contributes to the first and second research objectives. In addition to further characterization of an AHS array in unsteady flow separation, the effect of the hair material properties on its dynamic response and how the hair dynamics influence the resultant moment at the base of the hair is studied. Here, we show that the hair output is independent of the hair dynamics and dominated by the surface forces from the viscous flow. This result indicates that inertial forces of the hair, and thus the hair dynamics, may be neglected in modeling the relationship between the flow velocity incident on the hair and the resultant mechanical response at its base. These results also justified the similarity between the linear algebraic hair model and finite element simulations presented in Chapter 2.

The third objective, the effect of hair geometry on output sensitivity, is presented in the manuscript contained in Chapter 4. Based on the physical analysis contained in Chapter 3, a simplified quasi-steady model of the hair is developed. The relative hair length to any boundary layer flow that maximizes hair output sensitivity is determined. The range of computed optimal hair lengths are shown to be in close agreement with measured biological values. These results support the hypothesis that bats use hair sensors for boundary layer detection and provide geometric guidelines for artificial hair sensor design.

The article in Chapter 5 contains a proof-of-principle study for the fifth objective: flow observer design with hair sensor arrays. Observer (and control) design for flow problems (in general distributed parameter systems) is not without its own set of theoretical and computational challenges. Here we use a new algorithm [13, 14]

to compute linear quadratic control laws for an unsteady Stokes-type flow. This methodology is successfully applied to an observer design with hair sensor arrays as an addendum to this thesis in Chapter 6. This work is concluded in Chapter 8 with a summary of the results and conclusions of each manuscript.

THE DETECTION OF UNSTEADY FLOW SEPARATION WITH BIOINSPIRED HAIR-CELL SENSORS

B. T. Dickinson,   J. R. Singler,   B. A. Batten

2.1 Abstract

Biologists hypothesize that thousands of micro-scale hairs found on bat wings function as a network of air-flow sensors as part of a biological feedback flow control loop. In this work, we investigate hair-cell sensors as a means of detecting flow features in an unsteady separating flow over a cylinder. Individual hair-cell sensors were modeled using an Euler-Bernoulli beam equation forced by the fluid flow. When multiple sensor simulations are combined into an array of hair-cells, the response is shown to detect the onset and span of flow reversal, the upstream movement of the point of zero wall shear-stress, and the formation and growth of eddies near the wall of a cylinder. A linear algebraic hair-cell model, written as a function of the flow velocity, is also derived and shown to capture the same features as the hair-cell array simulation.

2.2 Introduction

Numerous reconnaissance and surveillance applications exist for autonomous micro-air-vehicles (MAV). However, the utility of the MAV is limited due in part to poor resistance to adverse pressure gradients and the formation of laminar separation bubbles that occur in their low-Reynolds number flight regimes. To mitigate the effects of such destabilizing flow phenomena, some researchers have sought to design closed-loop flow controllers, which when implemented on an MAV will require novel flow sensors due to payload and power limitations. In this work, we investigate a means of flow detection by drawing biological inspiration from the extraordinarily complex and extremely maneuverable flight of the bat.

Biologists have recently provided new evidence to suggest that thousands of hair-

cells (see Figure 2.1), scattered across the bat wing surface are actually a distributed sensing network that provides boundary layer feedback as part of a biological flow control loop [2]. The hair-cells shown in Figure 2.1 belong to the grey-headed flying-
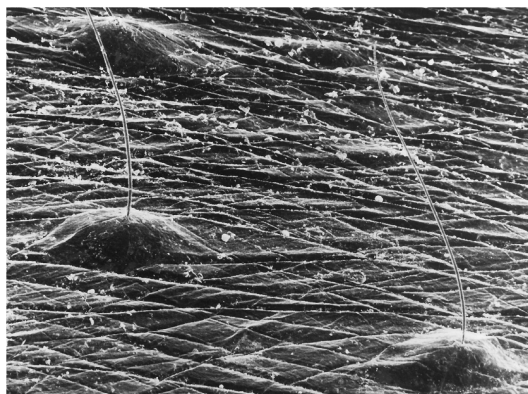
Figure 2.1: Scanning electron micrograph of hair cells on the wing of the grey-headed flying-fox (Reproduced by permission of CSIRO PUBLISHING, from the Australian Journal of Zoology vol. 42(2):215-231 (GV Crowley and LS Hall). Copyright CSIRO 1994. http://www.publish.csiro.au/nid/91/issue/2300.htm)

fox and are thought to be air-flow sensors [1]. The hairs are on the order of 1 mm tall, and protrude from dome structures which contain touch-sensitive cells. Apart from the bat, hair-cell arrays are also found in cartilaginous and bony fishes, where they are implicated in prey detection and tracking, collective schooling behavior, and maintaining position and orientation in strong currents [4]. Interestingly, hair-cells are also thought to play a role in boundary layer detection for locomotion control in fish. Other examples of hair cell use include movement sensitive touch detection in spiders [15] and sound vibration detection in mammals.

For controller implementation, new micro-electro-mechanical manufacturing technology is changing the hair-cell from a biological curiosity into an available sensor. Inspired by the biological hair-cell, the Micro Nano Technology Research (MNTR)

group[1] has designed, manufactured, and tested high sensitivity artificial hair-cell (AHC) sensors [16, 17, 18]. One AHC design is composed of an all-polymer hair attached to a force sensitive resistor base, as shown in Figure 2.2. Additionally, the
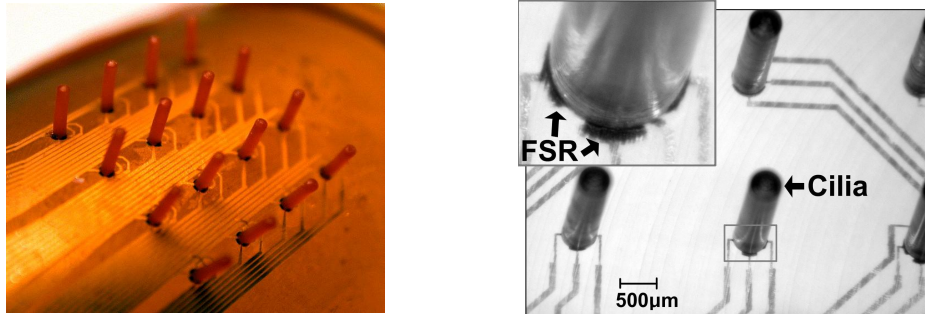
Figure 2.2: Photo of polymer artificial hair cell sensor (left) and force sensitive resistor (FSR) at base of polymer AHC (right). *Figures courtesy of C. Liu and group, MNTR lab, Northwestern University*

AHC may be manufactured as small as 10 μm in diameter.[2]

The design of a model-based controller with an array of hair-cell sensors will require an accurate model of the sensor array. In our previous work [19], a physical model for an individual AHC was developed, based on those manufactured by the MNTR group [17]. Here, we will investigate the response of an AHC array to unsteady flow separation and derive a linear algebraic model for a hair-cell array for application in linear control designs.

In the next section, we develop our model of the hair-cell sensor and state its assumptions. The flow and sensor array problem statement is presented in Section 2.4, followed by the results of the flow and hair-cell simulations in Section 2.5. In Section 2.6, a linear sensor model is derived and its response is compared to our sensor array simulations. Finally, we summarize our findings and outline avenues of future research in Section 2.7.

---

[1]Formerly at the University of Illinois at Urbana Champaign (UIUC), now at Northwestern University

[2]Private communication with Chang Liu, Northwestern University

2.3 Hair-Cell Model

When placed in an air flow, the biological hair-cell is subject to a net drag force that acts normal to its length, causing the output of bioelectrical signals from the hair-cell dome. With similar function, artificial hair-cell (AHC) designs have integrated micro-electro-mechanical mechanisms in their base [16, 17, 18]. In this work, we take the sensor's output as the bending moment at its base and note that future models of particular AHC designs may require additional modeling of electromechanical mechanisms.

To describe the relationship between the external flow around a hair-cell and the resulting bending moment, we use an Euler-Bernoulli beam equation coupled to a constitutive drag force equation. Viscoelastic material damping is also included with the Kelvin-Voigt material model. This leads to the following partial differential equation to describe the dynamics of each hair sensor

$$\rho_s A r_{tt}(t,\xi) + \gamma I r_{t\xi\xi\xi\xi}(t,\xi) + EI r_{\xi\xi\xi\xi}(t,\xi) = g(t,\xi), \quad 0 < \xi < L, \quad 0 < t < T, \quad (2.1)$$

with boundary conditions

$$r(t,0) = 0, \quad r_\xi(t,0) = 0,$$
$$EI r_{\xi\xi}(t,L) + \gamma I r_{t\xi\xi}(t,L) = 0, \quad EI r_{\xi\xi\xi}(t,L) + \gamma I r_{t\xi\xi\xi}(t,L) = 0, \qquad 0 < t < T,$$

and initial condition

$$r(0,\xi) = r_0, \quad 0 \le \xi \le L,$$

where $r(t,\xi)$ denotes the deflection of the hair at time t and position ξ, L is the hair's length, d is its diameter, ρ_s is the density of the hair-cell, A is its cross-sectional area, E is Young's modulus of the hair material, I is the moment of inertia, γ is the

Kelvin-Voigt coefficient of material damping, and $g(t,\xi)$ is the load intensity, with units of force per unit length. Additionally, the subscripts $(\cdot)_\xi$ and $(\cdot)_t$ denote partial derivatives.

To express the load intensity, $g(t,\xi)$, due to the flow we use the drag force equation

$$g(t,\xi) = \text{sgn}(u_n(t,\xi))\,\frac{1}{2}\,C_f(u_n)\,\rho_a\,d\,u_n(t,\xi)^2, \tag{2.2}$$

where $u_n(t,\xi)$ is the fluid velocity field projected normal to the length of the hair, $\text{sgn}(u_n)$ accounts for the direction of $u_n(t,\xi)$, ρ_a is the density of air, and C_f is the drag coefficient for a cylinder in cross flow, which was computed pointwise along the length of the sensor to account for the nonuniform velocity boundary layer.

A relationship between C_f and u_n was determined by fitting a first-order polynomial to the logarithm of empirical drag coefficients for an infinite cylinder versus Reynolds number as

$$\ln C_f(u_n) \approx -0.67\,\ln \text{Re}_\ell(u_n) + 2.51, \tag{2.3}$$

where the $\text{Re}(u_n)$ is a function of $u_n(t,\xi)$ and based on the hair's diameter as

$$\text{Re}_\ell(u_n) = \frac{u_n(t,\xi)\,d}{\nu}. \tag{2.4}$$

The drag coefficient equation (3.7) is an accurate approximation for $\text{Re}_\ell < 7$.

Finally, the moment at the base of the hair-cell may be computed as

$$M(t) = EIr_{\xi\xi}(t,0) + \gamma Ir_{t\xi\xi}(t,0). \tag{2.5}$$

In constructing the hair-cell model (2.2), we neglect any forces on the sensor from

flow phenomena on its free end, such as recirculation at the tip. Additionally, we do not account for any flow effects at the base of the sensor, such as a horseshoe vortex. By examining orders of magnitude in the Reynolds number expression (2.4), we find that for air passing over a hair-cell with $L = 1$ mm and $d = 10$ μm (the dimensions used herein), $\mid u_n(t, \xi) \mid \sim \text{Re}_\ell$. Thus, for $u_n << 1$, we have $\text{Re}_\ell << 1$ and the flow over the sensor will be very smooth. By limiting the sensor's height to 1 mm, so that it remains submerged within the boundary layer of our simulations, we ensure that $u_n(t, \xi) << 1$ m/s. Additionally, the immersion of the sensor in the boundary layer may help ensure its sensitivity to the boundary layer flow while the hair's protrusion into the freestream may saturate its response.

We also assume the effect of the sensor on the surrounding flow field is negligible. Thus, we couple the sensor to the flow through the load intensity, $g(t, \xi)$, but do not couple the flow to the sensor in the Navier-Stokes equations. Although, the true extent of the sensor's effect on the flow is unknown, preliminary wind tunnel experiments performed at Oregon State University with hair-cells mounted on the surface of micro-air-vehicle wings have supported this assumption.[3]

Finally, we assume that the velocity of any point on the sensor is much less than the flow velocity acting at that point, that is $r_\xi(t, \xi) << u_n(t, \xi)$ for $0 \leq \xi \leq L$ and $0 \leq t \leq T$. To this end, we do not compute a relative normal flow velocity due to the sensor's motion.

2.3.1 Discretization of Sensor Model

In this section, we describe the discretization of the hair-cell sensor model (2.1) with the finite element method. To compute approximate solutions, $r(\cdot, \cdot)$, we multiply

---

[3]Private communication with Dan Morse, Oregon State University

the sensor model (2.1) by a test function $\phi(\cdot)$ and integrate by parts twice to look for solutions $r(\cdot, \cdot) \in L^2(0, T; X(0, L))$ such that

$$\rho A \left(r_{tt}, \phi\right) + \gamma I \left(r_{t\xi\xi}, \phi_{\xi\xi}\right) + EI \left(r_{\xi\xi}, \phi_{\xi\xi}\right) - (g, \phi) = 0, \quad \forall \phi \in X(0, L), \quad (2.6)$$

where $X(0, L) = \{\phi \in H^2(0, L) \mid \phi(0), \phi_\xi(0) = 0\}$, and $(f, g) = \int_0^L f(x) \, g(x) \, dx$ denotes the standard L^2 inner product. In the finite element discretization of (3.12), we look for approximate solutions $r^h \in X^h$ such that

$$\rho A \left(r_{tt}^h, \phi^h\right) + \gamma I \left(r_{t\xi\xi}^h, \phi_{\xi\xi}^h\right) + EI \left(r_{\xi\xi}^h, \phi_{\xi\xi}^h\right) - \left(g, \phi^h\right) = 0, \quad \forall \phi^h \in X^h, \quad (2.7)$$

where $X^h \subset X(0, L)$ is a finite dimensional space spanned by cubic B-splines on a grid defined over $(0, L)$ and

$$r(t, \xi) \approx r^h(t, \xi) = \sum_{i=1}^{N} R_i(t) \phi_i(\xi).$$

Substituting r^h into the finite element form (3.13) gives the second-order system of ordinary differential equations (ODE)

$$M \, R'' + A \, R' + C \, R = F(t) \tag{2.8}$$

to be solved for $R = [R_1(t) \ldots R_N(t)]$, where $(\cdot)'$ denotes a time derivative. The ODE system (3.14) was set up as a system of first order equations in $[R, R']$ and solved using a backward differentiation formula (BDF) method. Implementation details are presented in Section 2.4.

2.4 The Problem Definition

The flow problem described here follows the impulsively started cylinder problem described by Gresho and Sani [20] (pages 794-845). Figure 2.3 illustrates the artificial flow domain, Ω, for a cylinder in cross flow used our simulations. Let $\mathbf{u}(t, \mathbf{x}) =$
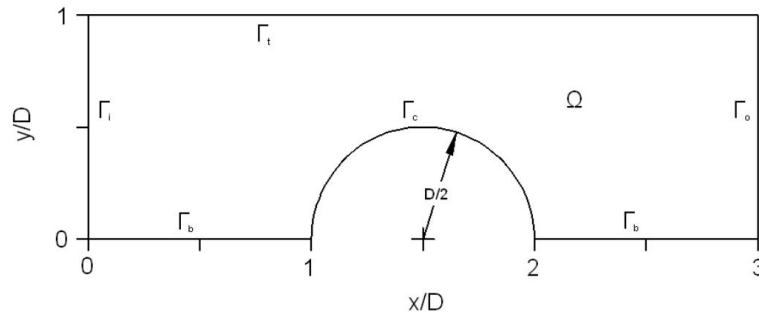
Figure 2.3: Fluid domain for unsteady fluid separation simulations performed in this analysis.

$[u(t, x, y), v(t, x, y)]$ denote the two-dimensional velocity field and $p(t, \mathbf{x})$ denote the pressure field which describe the fluid dynamics in Ω, modeled by the nondimensional viscous, incompressible Navier-Stokes equations

$$\mathbf{u}_t + \mathbf{u} \cdot \nabla \mathbf{u} = \nabla p + \frac{1}{\text{Re}} \nabla^2 \mathbf{u}$$
$$\nabla \cdot \mathbf{u} = 0$$

(2.9)

with the following initial and boundary conditions,

$$
\begin{aligned}
u = (1 - e^{-\lambda t}),\ v = 0 &\qquad \text{on} \qquad \Gamma_i &\times\ & (0, T], \\
-p\,\mathbf{n} + \frac{1}{\text{Re}} \frac{\partial \mathbf{u}}{\partial \mathbf{n}} = 0 &\qquad \text{on} \qquad \Gamma_o &\times\ & (0, T], \\
\frac{\partial u}{\partial \mathbf{n}} = 0,\ v = 0 &\qquad \text{on} \qquad \Gamma_{t,b} &\times\ & (0, T], \\
\mathbf{u} = 0 &\qquad \text{on} \qquad \Gamma_c &\times\ & (0, T], \\
\mathbf{u}(0, \mathbf{x}) = 0 &\qquad \text{in} \qquad \Omega, &&
\end{aligned}
$$

where the Reynolds number, Re, is

$$\mathrm{Re} = \frac{U\,D}{\nu},$$
(2.10)

U is a maximum inlet velocity, D is the diameter of the cylinder, and ν is the kinematic viscosity of air.

The time dependent boundary condition at the inlet accelerates the uniform inlet flow to a maximum velocity U according to the parameter λ. A "do nothing" boundary condition was selected at the outlet [21], symmetry boundary conditions were imposed on the top and bottom boundaries, and a no-slip condition was defined on the surface of the cylinder.

To solve the fluid problem, we used the two-dimensional Freefem++ finite element software [22]. We entered the fluid properties of air at 300K with $\rho = 1.161$ kg/m^3 and $\mu = 184.6 \times 10^{-7}$ N $\cdot$ s/m^2. The cylinder diameter, D, was 0.10 m and the steady inlet velocity value, U was selected as 0.03972 m/s for a Reynolds number of 250. The inlet acceleration parameter was $\lambda = -15$, which accelerated the inlet uniform flow from 0 to U m/s in approximately 0.5 seconds.

The Navier-Stokes equations were discretized with the Taylor-Hood pair and integrated with a constant time step of 1/10000 seconds over the time interval $0 \leq t \leq 5$ seconds with a first-order backward-step method. The domain was meshed with an unstructured triangulation containing 30532 elements in the pressure grid, and 59943 elements in the velocity grid. Grid independence of the flow simulation was supported after the above simulation was performed with approximately half the elements with identical results.

Following the fluid simulation above, the response of 179 equally spaced hair-cells on the surface of the cylinder was simulated. Sensors were numbered 1 through 179
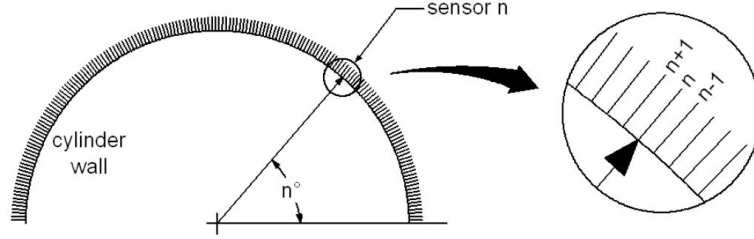
Figure 2.4: Illustration of hair-cell numbering scheme where 179 sensors were placed at n = 1, 2 ..., 179 degrees measured from the horizontal plane (sensors not shown to scale)

corresponding to their angular positions on the cylinder, as illustrated in Figure 3.3.

The finite element discretization of the sensor model (see Section 2.3.1) was implemented in MATLAB with 64 equally spaced nodes (verified grid independent) along the sensor with cubic B-splines used for basis and test functions. We integrated the resulting ODE system with MATLAB's built in solver `ode15s` for $0 \leq t \leq 5$ s. The `ode15s` package is a numerical differentiation formula routine with relative and absolute error tolerances set to 10^{-3} and 10^{-6}, respectively.

For each sensor, the load intensity, $g(t, \xi)$, was determined before the sensor simulation, by computing $u_n(t, \xi)$ for each hair-cell at 100 equally spaced points for $0 < \xi \leq L$ and 501 equally spaced points in time for $0 \leq t \leq 5$. During the integration of the discretized sensor model (2.8), $g(t, \xi)$ was interpolated with cubic splines to reconstruct the forcing vector, $F(t)$, at each time step.

Material parameters of the sensor for density, ρ_s, and Young's modulus, E, were chosen based on tabular values for polymers [23]. Table 2.1 lists the geometric and material parameters used herein. To our knowledge, tabular data for Kelvin-Voigt material damping, γ, of polymers is not available. However, our experiments with individual sensors show that while the deflection, $r(t, \xi)$, and velocity, $r_\xi(t, \xi)$, of the sensor are sensitive to changes in γ; the moment at the base, $M(t)$, gives virtually the same response for $1 \times 10^5 \leq \gamma \leq 1 \times 10^9$. Additionally, the sensor output $M(t)$ is

Table 2.1: Geometric and material parameters of the hair-cell sensor model (2.2)

Parameter	Value
L	1×10^{-3} m
d	1×10^{-5} m
ρ_s	1×10^3 kg/m^3
E	1×10^8 N/m^2
γ	1×10^8 N·s/m^2

shown to closely follow the tip load intensity $g(t, L)$, for $1 \times 10^5 \leq \gamma \leq 1 \times 10^9$, which

in this flow, generally represents the shape of $g(t, \xi)$, at for $0 \leq \xi \leq L$ for all time.

2.5   Results and Discussion

In this section, we discuss the response of the hair-cell sensor array to the flow simulation described in Section 2.4. In the flow simulation, an initially quiescent flow field is accelerated across the cylinder from the impulse-like inlet condition. Flow reverses direction on the downstream side of the cylinder in a initially very thin region near the wall. As time increases, a counterclockwise rotating eddy forms near the wall and convects downstream.

Figures 2.5, 2.6, 2.7, and 2.8 are nondimensional velocity magnitude plots of this simulation at $t = 0.50$, 2.00, 3.50, and 5.00 seconds, respectively. Figure 2.5 shows the boundary layer still fully attached at $t = 0.50$ s; however, at $t = 0.55$ s, the onset of flow reversal is observed in a thin layer near the wall on the order of 1×10^{-4} meters thick. As time increases from 0.50 to 2.00 s, the span of reversed flow at the cylinder wall increases to 66.5° (angles presented here are measured from the horizontal plane at the downstream side of the cylinder, as shown in Figure 2.4). Flow reversal near the wall is associated with a clockwise rotating eddy that forms during separation.
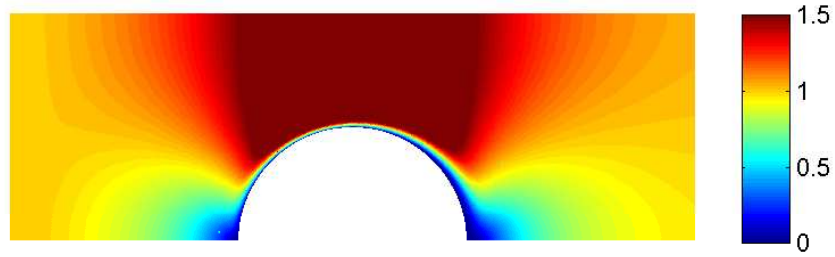
Figure 2.5: Nondimensional velocity magnitude snapshot at t = 0.50 s with the flow attached everywhere
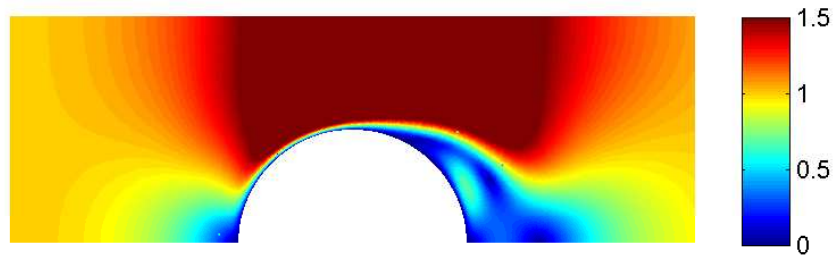
Figure 2.6: Nondimensional velocity magnitude snapshot at t = 2.00 s with reversed flow and point of zero wall shear at 66.5°
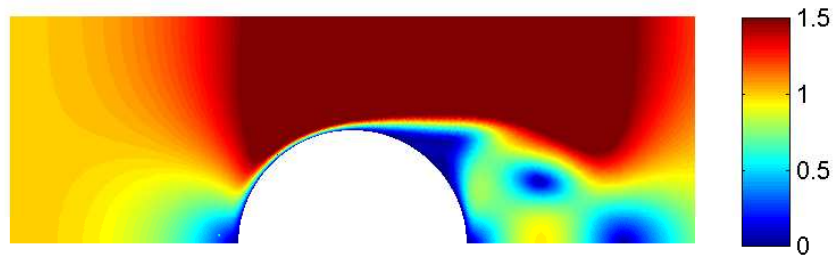
Figure 2.7: Nondimensional velocity magnitude snapshot at t = 3.50 s with reversed flow and point of zero wall shear at 68.3°
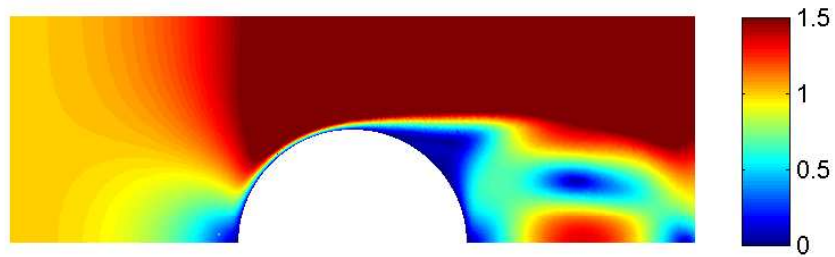
Figure 2.8: Nondimensional velocity magnitude snapshot at t = 5.00 s with reversed flow and point of zero wall shear at 68.6°
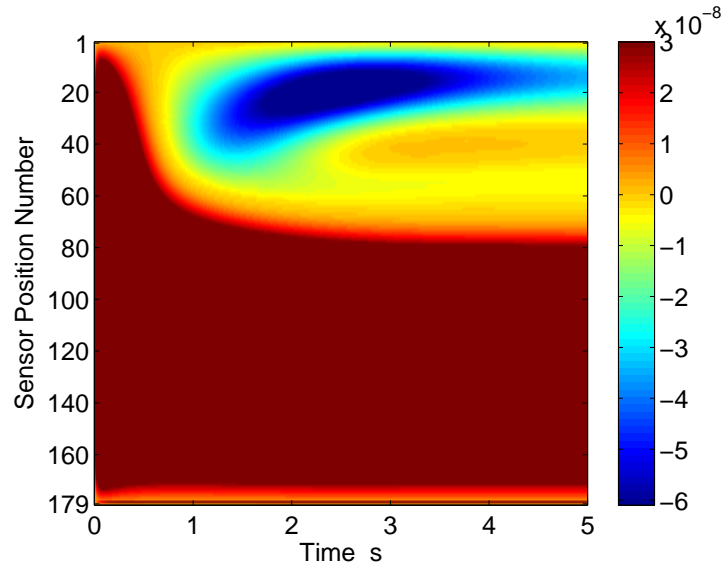
Figure 2.9: Image plot of the 179 hair-cell sensor array response to the separating flow simulation plotted against sensor position number and time showing

The eddy is shown to convect downstream as time increases. At $t = 5.00$ s, the reversed flow at the cylinder wall spans $66.8°$.

We now present the 179 hair-cell sensor array response to the unsteady separating flow. Figure 2.9 is an image plot of the moments $M(t)$ for the sensor array versus sensor position and time. The vertical axis contains the sensor position number with position 1 and 179 located at the top and bottom of the axis, respectively. Thus, the top half of the plot represents the sensor array output on the downstream side of the cylinder. To observe features in the array response to the unsteady separating flow, we limit the colorscale map of moment values to $-6.0 \times 10^{-8} \leq M(t) \leq 3.0 \times 10^{-8}$ mN·mm.

Close examination of the data in Figure 2.9 reveals the onset of reversed flow from the negative moment values on the order of 10^{-11} mN·mm near sensor 5 at $t = 0.59$ s, indicating the formation of an eddy on the downstream side of the cylinder. The reversed flow grows to span approximately 65 sensors at $t = 2.00$ s. Just beyond

the 65th sensor, we observe an interface between positive and negative moments, which corresponds to flow reversal or the instantaneous point of zero wall shear. The reader can verify that points of zero wall shear-stress noted in the fluid simulation snapshots, Figures 2.6, 2.6, 2.7, and 2.8, are in agreement with positive-negative moment interface, shown in the hair-cell array response, Figure 2.9.

The values of negative sensor moment come to a global minimum of -7.5×10^{-8} mN·mm at $t = 2.45$ s at sensor 19, which is due to the growth of the clockwise eddy. As time increases, minimum sensor moment increases and shifts toward sensor 1. At $t = 5.00$ s, the minimum sensor output is -3.5×10^{-8} mN·mm at sensor 14. The increase in minimum negative moment with time is a result of the downstream convection of the eddy.

Interestingly, at $t = 2.5$ s, a region of increasing moment near sensor 40 emerges and continues to increase until the sensor outputs a positive moment of 1.6×10^{-10} mN·mm at $t = 2.99$ s. From sensor 42 at $t = 2.99$ s, a region of positive moment grows to span sensors 38 to 44 at $t = 3.55$ s where a local maximum moment of 6.7×10^{-10} mN·mm by sensor 41 is observed. For $t > 3.55$ s, both the span and value of the positive moment region decreases, until the last positive moment is output by sensor 40 at $t = 4.59$ s. Although, not observed in the original postprocessing of the flow simulation, this region of positive moment indicates a small counterclockwise eddy centered near sensor 41, as shown in Figure 2.10.

Figure 2.10 is a vector velocity plot superimposed on nondimensional velocity magnitude spanning $30°$ to $70°$ near the cylinder wall at $t = 3.50$ s. Here, we observe a region of counterclockwise recirculation between the $35°$ and $50°$ mark. Upstream of the $50°$ mark, the flow is again reversed, which is part of the large downstream clockwise eddy that manages to flow over the small clockwise eddy. At the $68°$ mark, the reversed flow comes to the point of zero-shear and its trajectories are guided in
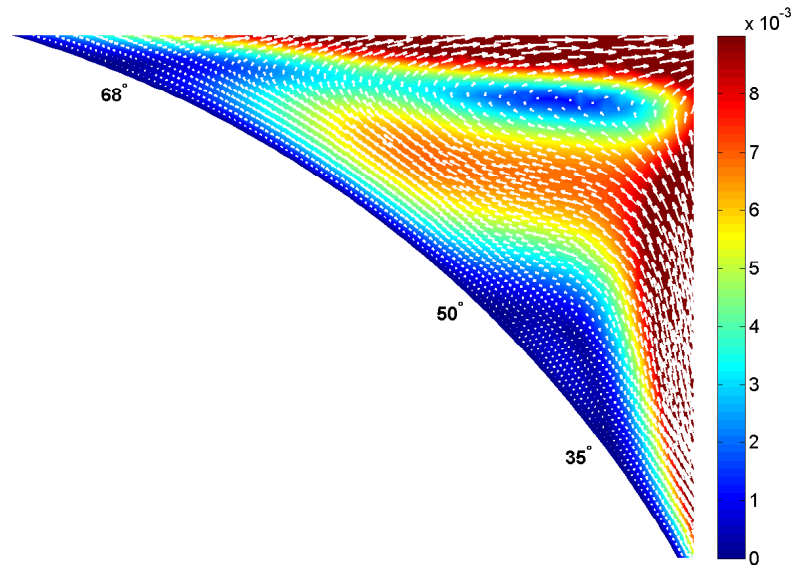
Figure 2.10: Vector velocity and velocity magnitude for $t = 3.50$ s near the cylinder wall spanning approximately 30° to 70° and showing the presence of a clockwise rotating eddy between the 35° and 50° marks that is trapped by the large downstream counterclockwise eddy

the downstream direction.

In closing this section, we remark that the hair-cell sensor array has revealed features of the unsteady separating flow with a surprising level of accuracy and detail. Both the onset and span of reversed flow were detected and were consistent with observations made in the flow simulation. The interface between positive and negative moments were also found to indicate points of zero wall shear stress. Additionally, the downstream motion of the eddy was observed from the sensor array response. Finally, the sensor array detected an unexpected counterclockwise eddy upstream of the large clockwise eddy, which was verified with subsequent reinspection of the flow simulation.

While a single hair-cell sensor can indicate flow direction; as hair-cells are assembled into a large array, a picture is painted from which we can observe detailed information on flow phenomena from measurements at the wall. On the basis of the
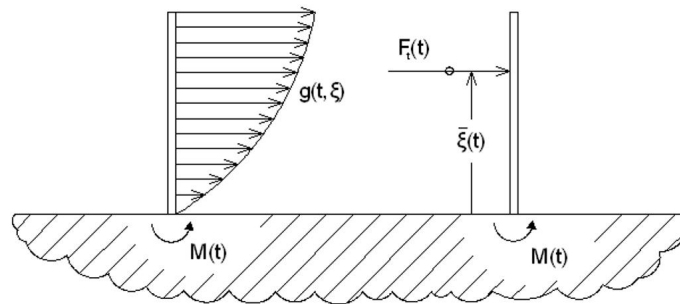
Figure 2.11: Load intensity, $g(t, \xi)$, acting on left sensor causing moment, $M(t)$, and equivalent point-load, $F_t(t)$, acting on the right sensor at the center of mass of $g(t, \xi)$, $\bar{\xi}(t)$, to produce the equivalent moment $M(t)$

above results, a hair-cell array appears to be a promising choice for detection of the boundary layer.

2.6 Linear Algebraic Sensor Model

Linear control theory is well developed with many tests available to verify the stability, robustness, and overall effectiveness of the controller. Although most fluid flows we wish to control are nonlinear, this does not necessarily preclude the successful application of a linear control design. For example, linear optimal control designs with linearized Navier-Stokes equations have been shown to successfully reduce wall shear in a turbulent flow [24].

In this section, we present a linear algebraic model of the hair-cell sensor array for application in linear flow controllers. Our derivation of an algebraic sensor model for the hair-cell sensor begins by expressing the load intensity $g(t, \xi)$ as a resultant drag force, $F_t(t)$, acting at height $\bar{\xi}(t)$ on the sensor, so that an equivalent moment $M(t)$ is produced at the base, as illustrated in Figure 2.11.

Following the point-load representation in Figure 2.11, we compute the output

$M(t)$ as

$$M(t) = F_t(t)\,\bar{\xi}(t) \tag{2.11}$$

where $F_t(t)$ is the total drag force acting on the sensor,

$$F_t(t) = \int_0^L g(t, \xi)\, d\xi \tag{2.12}$$

and $\bar{\xi}(t)$ is determined by the center of mass of the load intensity $g(t, \xi)$ as,

$$\bar{\xi}(t) = \frac{\int_0^L g(t, \xi)\, \xi\, d\xi}{\int_0^L g(t, \xi)\, d\xi}. \tag{2.13}$$

The substitution of (2.12) and (2.13) into (2.11) gives the following equation for moment

$$M(t) = \int_0^L g(t, \xi)\, \xi\, d\xi. \tag{2.14}$$

Recall the expression for $g(t, \xi)$ (2.2), presented in Section 2.3 as

$$g(t, \xi) = \mathrm{sgn}(u_n(t, \xi))\, \frac{1}{2}\, C_f(u_n)\, \rho_a\, d\, u_n(t, \xi)^2. \tag{2.2}$$

where

$$\ln C_f(u_n) \approx -0.67\, \ln \mathrm{Re}_\ell(u_n) + 2.51 \tag{2.3}$$

and

$$\mathrm{Re}_\ell(u_n) = \frac{u_n(t, \xi)\, d}{\nu}. \tag{2.4}$$

When equations (2.2), (2.3), and (2.4) are combined, the sensor moment output $M(t)$ may be written as

$$M(t) = 6.15\, \rho_a\, d^{0.33}\, \nu^{0.67} \int_0^L \mathrm{sgn}(u_n(t, \xi))\, \mid u_n(t, \xi) \mid^{1.33}\, d\xi. \tag{2.15}$$

Note that the integrand appearing in (2.15) is nonlinear. To linearize (2.15), a least squares fit with a first-order polynomial was performed for $-0.0075 \leq u_n(t, \xi) \leq 0.0075$ m/s to obtain the linear expression for moment

$$M(t) = 1.12 \, \rho_a \, d^{0.33} \, \nu^{0.67} \int_0^L u_n(t, \xi) \, d\xi. \tag{2.16}$$

The interval $-0.0075 \leq u_n(t, \xi) \leq 0.0075$ m/s was chosen through trial-and-error to give the most identical results to the hair-cell sensor array simulation in Figure 3.16 of the previous section. To compute with (2.16), the integral may be approximated with quadrature or some other numerical integration procedure. Here we used the Riemann sum so that

$$M(t) = \sum_{i=1}^N c_i \, u_n(t, \xi_i) \tag{2.17}$$

and

$$c_i = 1.12 \, \rho_a \, d^{0.33} \, \nu^{0.67} \, \xi_i \, \Delta \xi \tag{2.18}$$

where ξ_i is the ith position along the sensor.

To assemble a linear algebraic model for an array of hair-cell sensors, equation (2.17) may be applied to each sensor and assembled in matrix form as,

$$\begin{bmatrix} M_1(t) \\ \vdots \\ M_N(t) \end{bmatrix} = \begin{bmatrix} c_{1,1} & \cdots & c_{1,M} & 0 & \cdots & 0 \\ \vdots & & \ddots & & & \vdots \\ 0 & \cdots & 0 & c_{N,1} & \cdots & c_{N,M} \end{bmatrix} \begin{bmatrix} u_n^1(t, \xi_1) \\ \vdots \\ u_n^1(t, \xi_M) \\ \vdots \\ u_n^N(t, \xi_1) \\ \vdots \\ u_n^N(t, \xi_M) \end{bmatrix}, \tag{2.19}$$
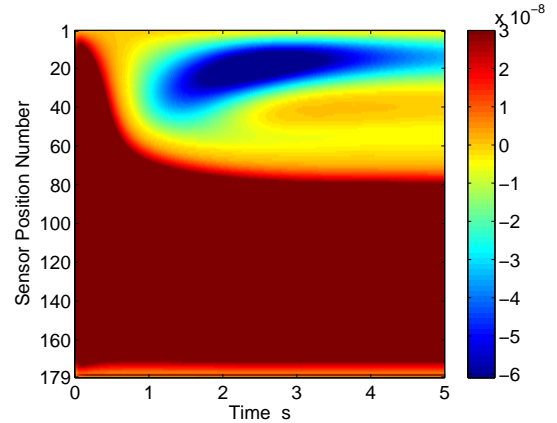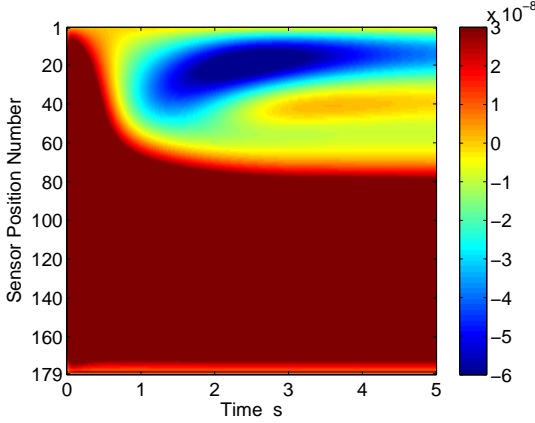
Figure 2.12: Sensor array response computed with linear algebraic model

Figure 2.13: Sensor array response from finite element simulation

where $M_i(t)$ is the moment output of the i*th* sensor, $c_{i,j}$ is the coefficient computed for i*th* sensor at ξ_j, and $u_n^i(t, \xi_j)$ is the normal velocity component acting on the i*th* sensor at the j*th* position.

Figure 2.12 is the sensor array response to the unsteady separating flow simulation computed with the linear algebraic model (2.19). Here, we also limit the colorscale map of moment values to $-6.0 \times 10^{-8} \leq M(t) \leq 3.0 \times 10^{-8}$ mN·mm. For comparison, the hair-cell array response described by partial differential equation model (2.1) and presented in Section 2.5 is reproduced to the right of the Figure 2.12. Based on the similarity between Figures 2.12 and 2.13, the linear algebraic sensor model accurately captures the hair-cell array input-output relationship of the finite-element simulations.

Future work will see the use of the above hair-cell model in model based flow-control designs with the Navier-Stokes equations. In particular, linear quadratic Gaussian (LQG) and extended LQG observers will be used estimate the flow field from the partial state information provided by a hair-cell array at the wall.

2.7   Summary

Biologists hypothesize that the thousands of hairs scattered across the bat wing is actually an air-flow sensing network and part of a biological feedback flow control loop. Here, a simulation of a hair-cell sensor array placed on a cylinder wall in an unsteady separating flow was performed.

Finite element simulations of a 179 hair-cell array revealed features of the unsteady separating flow with a surprising level of accuracy and detail. Observations between the output of the hair-cell array and the flow simulation showed that the hair-cell array detected both the onset and span of reversed flow, the movement of the point of zero wall shear, the downstream convection of an eddy, and the formation of a small counterclockwise eddy upstream of the larger clockwise eddy. Additionally, a linear algebraic sensor model was derived and shown to accurately reproduce the hair-cell array response from the finite element simulations.

Future work will see the application of the linear hair-cell model to linear control designs with the Navier-Stokes equations. In particular, linear quadratic Gaussian (LQG) and extended LQG observers will be constructed and the ability of a hair-cell array to estimate the flow features in the boundary layer from limited velocity information at the wall will be investigated.

MATHEMATICAL MODELING OF BIOLOGICALLY INSPIRED HAIR RECEPTOR ARRAYS IN LAMINAR UNSTEADY FLOW SEPARATION

B. T. Dickinson,   J. R. Singler,   B. A. Batten

3.1 Abstract

Many animals use hair-like structures to detect fluid flows. Bats fly at low Reynolds numbers so they must be able to detect and react to unsteady flows across their wings to maintain control. Studies have shown that bats have arrays (0.10 to 4.0 mm in length) of hair receptors distributed across the wing membrane surfaces. The hair array is hypothesized to detect flow fields near the wing, enabling the bat to adjust its wing shape and kinematics to maintain stability during flight, and while performing complex maneuvers. Micro air vehicles (MAV) are also low Reynolds number flyers and subject to unsteady flow structures that can determine flight stability. This work was inspired by the bat hair receptor array as a potential sensing system to control destabilizing flows over a MAV wing. Our objectives were to characterize hair receptor dynamics to unsteady viscous flows and determine what features of laminar unsteady flow separation could be detected by an array of hairs. Finite element simulations of a viscoelastic hair model showed that surface forces from the viscous airflow dominated the hair dynamics, and the moment at the base of the hair provided a time accurate indication of local flow direction and magnitude. The set of moments from an array of hairs in unsteady flow separation accurately indicated the location of the point of zero wall shear stress, the formation and movement of near wall eddies, and the span of reversed flow. These results support the utility of artificial hair sensor arrays for flow controller designs in the MAV, and are consistent with the hypothesis that bats use hair receptor arrays to detect unsteady flow patterns.

3.2   Introduction

Many animals use hair-like structures to detect their environments. Cartilaginous and bony fishes use hair sensory arrays for prey detection and tracking, collective schooling behavior, and maintaining position and orientation in strong currents [4]. Mammals and non-mammalian vertebrates detect sound aided by bundles of hair cells contained in the cochlea [25]. Other examples of hair sensors include flow detection in crickets [26] and movement sensitive touch detection in spiders [15].

Recent studies have shown that bats also have hair receptors, 0.10 to 4.0 mm in length, growing from the dorsal and ventral wing surfaces [1, 2, 27, 3]. Figure 3.1 shows hair receptors belonging to the gray-headed flying fox (*Pteropus poliocephalis*) which protrude from hair receptor domes that contain touch sensitive cells. Biologists
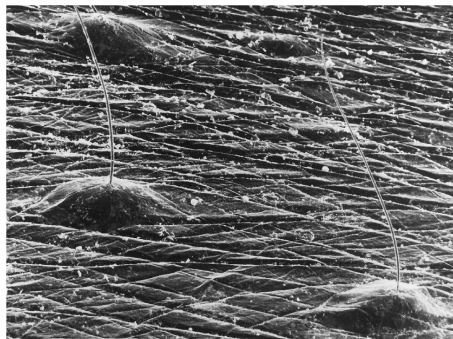
Figure 3.1: Scanning electron micrograph of hair receptors on the wing membrane of *Pteropus poliocephalis* (the grey-headed flying-fox) (Reproduced by permission of CSIRO PUBLISHING, from the Australian Journal of Zoology vol. 42(2): 215-231 (GV Crowley and LS Hall). Copyright CSIRO 1994 .http://www.publish.csiro.au/nid/91/issue/2300.htm)

hypothesize that the hair receptors are used to sense airflow patterns from the wing surface as part of a biological closed loop flow control system [3]. The bat is thought to change its wing shape in response to detected flow patterns in their highly unsteady low Reynolds number regimes of flight.

Like the bat, the micro air vehicle[1] (MAV) is low Reynolds number flyer. Although numerous reconnaissance and surveillance applications exist for the autonomous MAV, its overall utility is limited due to destabilizing aerodynamic forces that occur in low Reynolds flight regimes [28, 29, 30]. One approach to improving flight stability is the integration of a flow control system in the MAV wing to detect and mitigate the effect of destabilizing flows. Such control designs are inherently limited to incomplete flow information, likely provided by a suite of surface mounted sensors.

In this work, we investigate the mechanical and dynamic response of an array of hairs to unsteady flow separation, which has important aerodynamic consequences for flight. Our objective was to determine if the mechanical responses output by an array of hair receptors were sensitive in space and time to characteristic phenomena of unsteady flow separation. By understanding how hair receptors detect unsteady laminar airflows, we aim to provide groundwork for the effective integration of artificial hair receptors [16, 17, 18, 31, 32, 33] (Figure 3.2) in flow control designs.
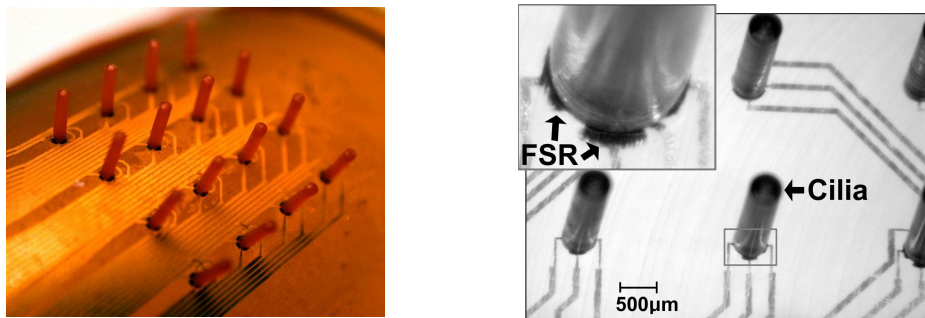
Figure 3.2: Photo of polymer artificial hair sensor (left) and force sensitive resistor (FSR) at base of polymer AHC (right). *Figures courtesy of C. Liu and group, MNTR lab, Northwestern University*

While limited information is available on bat wing hair receptors, the modeling and simulation of cochlear hair cells has been performed [34, 35]. Cochlear hair cells are smaller than bat hair receptors (up to two orders of magnitude in length

---

[1]A micro air vehicle is loosely defined as an aircraft with wingspan on the order of 10^{-1}m or less

and diameter) and exist in a fluid known as endolymph. Estimates of the Reynolds number for endolymph flow over a cochlear hair cell range from 10^{-2} to 10^{-3}, leading to models of the endolymph fluid environment with Stokes equations. Based on measurements of bat flight speeds [36] ($\sim$ 10m/s) and bat hair receptor diameters [1] ($\sim$ 10μm), we estimate hair receptor Reynolds numbers on the order of 10^0, which violates the "massless" flow assumption of Stokes equations.

To investigate the dynamic response of hair receptors to laminar unsteady flow separation we modeled each hair with an Euler-Bernoulli beam equation coupled to the flow with solution data from the Navier-Stokes equations. Simulations of hair receptors indicated that hair receptor dynamics were dominated by surface forces from the flow. A similar result has been reported for cochlear hair cells [34, 37, 35].

Since the forces on the hair were dominated by the flow, the moment at the base (output) of the hair provided a reasonably time accurate indication of local flow direction and magnitude. As a result, hair receptor arrays provided a surprisingly accurate picture of the flow from the wall. Specifically, the hair array was shown to detect the onset and span of regions of reversed flow, the location of the point of zero wall shear stress, and the formation and movement of a near wall eddies. These results support the utility of artificial hair receptors for engineered flow control designs and are consistent with the hypothesis that bats use hair receptors for flow detection.

3.3 Mathematical Modeling of the Hair/Fluid Problem

Here we consider an array of hairs placed at angles 1°, 2°, ..., 179° on a cylinder (Figure 3.3) that is impulsively started from rest in quiescent air. Unsteady flow separation is known to occur on the downstream side of the impulsively started cylinder [38].
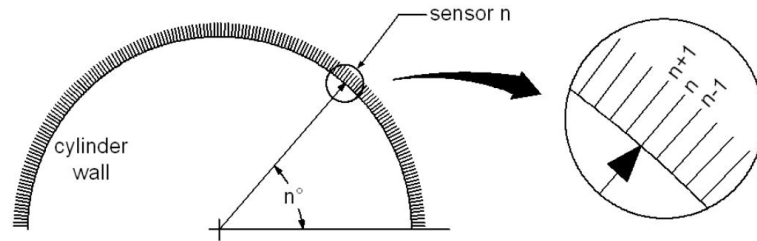
Figure 3.3: Illustration of hair sensor array position and numbering where sensors are placed at n = $1°, 2° \ldots, 179°$ measured from the horizontal plane (sensor length and diameter are not shown to scale)

A reasonable diameter for hair receptors found on bat wings (and used for simulations herein) is 1×10^{-5}m. Given the hair is subject to airflows up to 10m/s, the local hair Reynolds number is on the order of 10^0. To experience this ratio of inertial to viscous forces, we would need to immerse ourselves in a pool of glycerin and swim at speeds on the order of 10m per hour! From this perspective we anticipate that inertial forces in the hair will be small. However, we include inertial terms in the hair model and let the results justify this expectation.

Each hair is modeled as a viscoelastic cantilever beam with uniform diameter and material properties; although, biological hair receptors observed on bat wings are tapered (Figure 3.1). Material damping and air damping from the viscous flow environment are included in the hair model.

We take the output of each hair as the resultant moment at its base because, as a cause of mechanical stress in the bat wing membrane, the resultant moment at the base of the hair could activate touch sensitive cells in the hair receptor dome [2]. The moment at the base of the hair could also activate micro-electro-mechanical devices in artificial hair sensors, such as the force sensitive resistor at the base of the polymer hair shown in Figure 3.2.

Although the true effect of the hair on the flow is unknown, we assume that the effect of the hair on the flow is negligible. Preliminary wind tunnel experiments

performed at Oregon State University with artificial polymer hairs mounted on the surface of micro-air-vehicle wings support this assumption[2].

The problem of computing the output of an array of hairs from a viscous unsteady airflow contains three main parts and is similar in approach to simulations performed for cochlear hair cells by [34]:

1. The simulation of the flow environment and the calculation of the flow velocity incident on the hair

2. The computation of the force per unit length acting on each hair and the dynamic response of the hair in the viscous flow

3. The calculation of the moment at the base (output) of the hair.

3.3.1 Flow Over an Impulsively Started Cylinder From Rest

Figure 3.4 illustrates the artificial flow domain, Ω, for the half-cylinder in cross-flow simulated herein. Let $\mathbf{u}(t^*, \mathbf{x}^*) = [u(t^*, x^*, y^*), v(t^*, x^*, y^*)]$ denote the two-
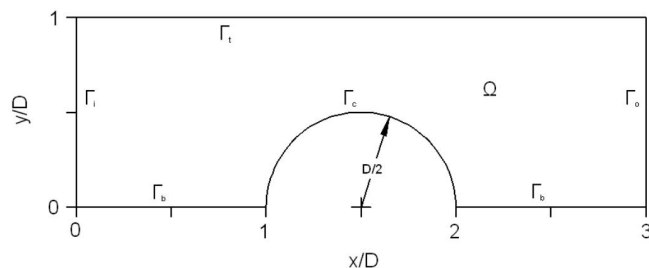
Figure 3.4: Fluid domain for unsteady fluid separation simulations performed in this analysis.

dimensional velocity field and $p(t^*, \mathbf{x}^*)$ denote the pressure field that describes the fluid dynamics in Ω, modeled by the nondimensional viscous, incompressible Navier-

---

[2]Private communication with Dan Morse, Oregon State University

Stokes equations

$$\mathbf{u}_t + \mathbf{u} \cdot \nabla \mathbf{u} = \nabla p + \frac{1}{\mathrm{Re}} \nabla^2 \mathbf{u}$$
$$\nabla \cdot \mathbf{u} = 0$$

(3.1)

with the following boundary and initial conditions,

$$
\begin{aligned}
u = (1 - e^{-\lambda t^*}),\ v = 0 &\qquad \text{on} \qquad \Gamma_i &\times& \quad (0, T], \\
-p\,\mathbf{n} + \frac{1}{\mathrm{Re}} \frac{\partial \mathbf{u}}{\partial \mathbf{n}} = 0 &\qquad \text{on} \qquad \Gamma_o &\times& \quad (0, T], \\
\frac{\partial u}{\partial \mathbf{n}} = 0,\ v = 0 &\qquad \text{on} \qquad \Gamma_{t,b} &\times& \quad (0, T], \\
\mathbf{u} = 0 &\qquad \text{on} \qquad \Gamma_c &\times& \quad (0, T], \\
\mathbf{u}(0, \mathbf{x}) = 0 &\qquad \text{in} \qquad \Omega, &&
\end{aligned}
$$

and Reynolds number,

$$\mathrm{Re} = \frac{U\,D}{\nu},$$

(3.2)

where U is a maximum inlet velocity, D is the diameter of the cylinder, and ν is the kinematic viscosity of air.

The time dependent boundary condition at the inlet Γ_i accelerates the uniform inlet flow to a maximum velocity U according to the parameter λ. The "do nothing" boundary condition [21] was imposed at the outlet Γ_o, symmetry boundaries were specified on the top Γ_t and bottom Γ_b of the domain, and a no-slip condition was set on the surface of the cylinder Γ_c.

3.3.2 Viscoelastic Hair Forced by a Viscous Flow

To describe the relationship between an external flow around a hair and the hair output, taken here as the moment at its base, we used a viscoelastic model of an Euler-Bernoulli beam coupled to flow with drag coefficients for a circular cylinder in

crossflow. Material damping was included with the Kelvin-Voigt model. This led to the following nonlinear partial differential equation to describe the dynamics of each hair receptor

$$\rho_s A r_{tt}(t,\xi) + \gamma I r_{t\xi\xi\xi\xi}(t,\xi) + EI r_{\xi\xi\xi\xi}(t,\xi) = g(r_t), \quad 0 < \xi < \ell, \quad t > 0, \qquad (3.3)$$

with boundary conditions for a cantilever beam

$$r(t,0) = 0, \quad r_\xi(t,0) = 0,$$
$$t > 0,$$
$$EI r_{\xi\xi}(t,\ell) + \gamma I r_{t\xi\xi}(t,\ell) = 0, \quad EI r_{\xi\xi\xi}(t,\ell) + \gamma I r_{t\xi\xi\xi}(t,\ell) = 0,$$

and initial condition

$$r(0,\xi) = r_0(\xi), \quad 0 \le \xi \le \ell,$$

where: r denotes the deflection of the hair from the neutral axis; ℓ is the hair length; ρ_s is the density of the hair; A is its cross-sectional area; E is Young's modulus of the hair material; I is the moment of inertia; γ is the Kelvin-Voigt coefficient of material damping; g is a force per unit length acting on the hair, known as the load intensity; and the subscripts $(\cdot)_\xi$ and $(\cdot)_t$ denote partial derivatives.

To compute the load intensity due to the flow we used the drag coefficient for a circular cylinder in crossflow as

$$g(t,\xi) = \text{sgn}(u_n(t,\xi)) \frac{1}{2} C_d(\text{Re}_\xi) \rho_a \, d \, u_r(t,\xi)^2, \qquad (3.4)$$

where d is the hair diameter (constant), ρ_a is the fluid density, and $u_r(t,\xi)$ is the relative flow velocity acting normal to the length of hair computed as

$$u_r(t,\xi) = u_n(t,\xi) - r_t(t,\xi) \qquad (3.5)$$

where $u_n(t, \xi)$ is the projection of the Navier-Stokes velocity data normal to the length of the hair sensor and $r_t(t, \xi)$ is the hair velocity.

Figure 3.5, contains a freebody diagram of the hair subject to a nonuniform incident flow profile.
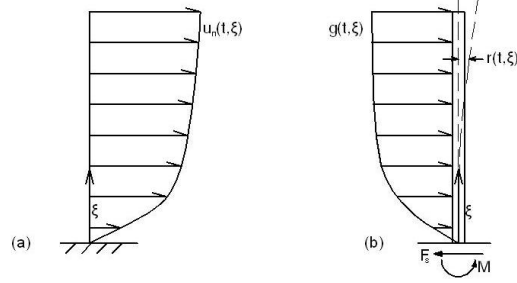
Figure 3.5: Nonuniform incident flow velocity (a) and corresponding freebody diagram (b) of a hair

To account for the nonuniform relative flow velocity, the drag coefficient, C_d, was computed as a function of the local Reynolds number

$$\mathrm{Re}_\xi = \frac{u_r(t, \xi)\, d}{\nu}. \tag{3.6}$$

We developed a relationship between C_d and Re_ξ by fitting a first-order polynomial to the logarithm of empirical drag coefficients for a circular cylinder in crossflow [19] for $0 < \mathrm{Re}_\xi \le 10$, as

$$\ln C_d(\mathrm{Re}_\xi) \approx -\frac{2}{3} \ln \mathrm{Re}_\xi + \frac{5}{2}. \tag{3.7}$$

Based on the hair model (3.3), the moment at the base of the hair (output) is given by the following expression

$$M(t) = EI r_{\xi\xi}(t, 0) + \gamma I r_{t\xi\xi}(t, 0). \tag{3.8}$$

We nondimensionalize the hair model (3.3) by introducing the following nondi-

mensional variables

$$\xi^* = \frac{\xi}{\ell}, \quad t_b^* = \tau\, t, \quad r^* = \frac{r}{\ell}, \quad d^* = \frac{d}{d_0}, \quad u_r^* = \frac{u_r}{U}$$

where d_0 is a reference hair diameter. The parameter $\tau = E/\gamma$ is known as the *rate of relaxation* and governs the rate that strain in a Kelvin-Voigt material with a constant applied stress comes to equilibrium [39]. Note that the inverse of the rate of relaxation, $1/\tau = \gamma/E$, is a time scale of the Kelvin-Voigt material.

When the above nondimensional variables are substituted into the hair sensor model (3.3) we obtain the following nonlinear partial differential equation

$$\tau^2\, m\, r^*_{t_b^* t_b^*} \;+\; \frac{EI}{\ell^3}\left(r^*_{t_b^* \xi^* \xi^* \xi^* \xi^*} \;+\; r^*_{\xi^* \xi^* \xi^* \xi^*} \right) = g_r \cdot g^*(r^*_{t_b^*}) \tag{3.9}$$

where $m = \rho_s\, A\, \ell$ is the mass of the hair, $g_r = \rho_a\, d_0\, U^2$ is the reference load intensity, and

$$g^*(r^*_{t_b^*}) = \frac{g}{g_r} = \frac{1}{2} C_d\left(d^*, u_r^*, \mathrm{Re}_0\right) d^*\, u_r^{*2}. \tag{3.10}$$

is the nondimensional load intensity. Recall that u_r^* depends on $r^*_{t_b^*}$ due to equation (3.5). Also, $C_d\left(\mathrm{Re}_\xi\right)$ in (3.4) has been replaced with $C_d\left(d^*, u_r^*, \mathrm{Re}_0\right)$ in (3.9) since

$$\mathrm{Re}_\xi = d^*\, u_r^*\, \mathrm{Re}_0$$

where

$$\mathrm{Re}_0 = \frac{U\, d_0}{\nu}$$

so that the forcing on the hair due to the flow may be written as a function of the nondimensional variables d^*, u_r^*, and Re_0.

In nondimensional form, the hair output becomes

$$M^* = \frac{M}{M_r} = r^*_{t_b^* \xi^* \xi^*}(t_b^*, 0) \; + \; r^*_{\xi^* \xi^*}(t_b^*, 0) \tag{3.11}$$

where $M_r = EI/\ell$.

3.4   Simulation Details

3.4.1   Finite Element Solution of the Fluid Model

Solutions to the flow problem (3.1) were approximated using the characteristic Galerkin finite element method [40] with the software package FreeFEM++ [22]. We set the cylinder diameter, $D = 0.10$m and maximum inlet velocity, $U = 0.0794$m/s for Re $=500$. The inlet acceleration parameter was $\lambda = 15$. We discretized in space with the Taylor-Hood pair and integrated with a constant time step of 10^{-5} seconds over the time interval $0 \leq Ut/D \leq 3.97$ with a first order backward-step method. The domain was meshed with an unstructured triangulation and refined at the cylinder wall to help resolve the flow velocity near the hair. The final grid was composed of 30532 elements in the pressure grid, and 59943 elements in the velocity grid.

3.4.2   Finite Element Solution of the Hair Model

To compute approximate solutions to $r^*(t_b^*, \xi^*)$, we multiplied the nonlinear hair model (3.9) by a test function $\phi(\xi^*)$ and integrated by parts twice to look for so-

lutions $r^*(t_b^*, \xi^*) \in L^2(0, T; V)$ such that

$$
\tau^2 m\left(r_{t_b^* t_b^*}^*, \phi\right) + \frac{EI}{\ell^3}\left(r_{t_b^* \xi^* \xi^*}^* + r_{\xi^* \xi^*}^*, \phi_{\xi^* \xi^*}\right) - \\
g_r\left(g^*(r_{t_b^*}^*), \phi\right) = 0, \quad \forall \phi \in V, \tag{3.12}
$$

where $V = \{\phi \in H^2(0, L) \,|\, \phi(0), \phi_\xi(0) = 0\}$, and $(f, g) = \int_0^L f(x)\, g(x)\, dx$ denotes the standard L^2 inner product. In the finite element discretization of (3.12), we looked for approximate solutions $r^{*h} \in V^h$ such that

$$
\tau^2 m\left(r_{t_b^* t_b^*}^{*h}, \phi\right) + \frac{EI}{\ell^3}\left(r_{t_b^* \xi^* \xi^*}^{*h} + r_{\xi^* \xi^*}^{*h}, \phi_{\xi^* \xi^*}^h\right) - \\
g_r\left(g(r_{t_b^*}^{*h}), \phi^h\right) = 0, \quad \forall \phi^h \in V^h, \tag{3.13}
$$

where $V^h \subset V$ is a finite dimensional space spanned by cubic B-splines $\{\phi(\xi^*)\}_{i=1}^N$ on a grid defined over $(0, L)$ and

$$
r^*(t_b^*, \xi^*) \approx r^{*h}(t_b^*, \xi^*) = \sum_{i=1}^N R_i(t_b^*)\phi_i(\xi^*).
$$

Substituting r^{*h} into the finite element form (3.13) gave the second-order system of nonlinear ordinary differential equations (ODE)

$$
M\,R'' + A\,R' + C\,R = F(t_b^*, R') \tag{3.14}
$$

to be solved for $R = [R_1(t_b^*) \dots R_N(t_b^*)]$, where $(\cdot)'$ denotes a time derivative.

The finite element discretization of the hair model was implemented in MATLAB with 64 equally spaced nodes (verified grid independent) along the hair. The resulting ODE system (3.14) was integrated with MATLAB's built in solver `ode15s` over $0 \leq t_b^* \leq 5$ where $F(t_b^*, R')$ was reconstructed at each time step. The `ode15s` package is a numerical differentiation formula routine. Relative and absolute error tolerances

were both set to 10^{-10}.

Material parameter values of the hair for density, ρ_s, and Young's modulus, E, were chosen based on tabular values for polymers [23], as listed in Table 3.1. The length and diameter of the hair were selected to be representative of hair receptor dimensions found on bat wings [1]. Due to a lack of tabular data for Kelvin-Voigt

Table 3.1: Geometric and material parameters used in the simulation of each hair

Parameter	Value
ℓ	10^{-3} m
d	10^{-5} m
ρ_s	10^3 kg/m^3
E	10^8 N/m^2
γ	$10^4 - 10^{10}$ N·s/m^2

material damping, γ, we investigate the dynamic response and output of a hair for $\gamma = 10^4 - 10^{10}$ N·s/m^2 in the following section.

3.5   Simulation Results and Discussion

3.5.1   Simulation of the Flow Over an Impulsively Started Cylinder

Figures 3.6, 3.7, and 3.8 are respective velocity magnitude plots of the flow simulation at $t^* = tU/D = 0.064, 0.40,$ and 1.19 showing the unsteady separation of the boundary layer on the downstream side of the impulsively started cylinder.

At $t^* = 0.064$, the flow is attached and symmetric (Figure 3.6). As t^* increases, an adverse pressure gradient forms, leading to the onset of reversed flow at $t^* = 0.25$ at the trailing edge of the cylinder. As the span of reversed flow at the cylinder wall grows, a clockwise eddy forms, as shown in Figure 3.8.

During the unsteady separation of the boundary layer, the point of zero wall shear stress is located at the point on the cylinder wall where the wall normal velocity
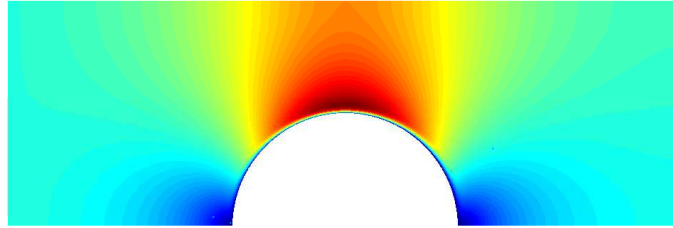
Figure 3.6: Nondimensional velocity magnitude snapshot at $t^* = 0.064$ with the flow attached everywhere
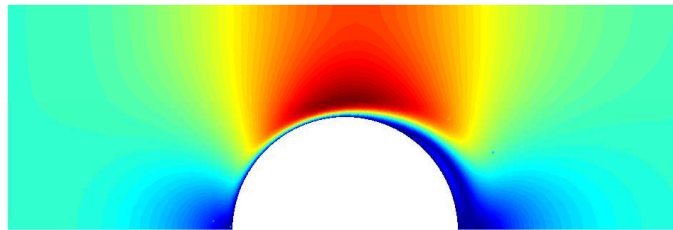
Figure 3.7: Nondimensional velocity magnitude snapshot at $t^* = 0.40$ with point of zero wall shear stress at 59.9°
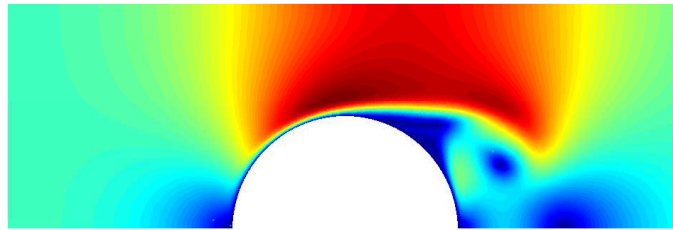
Figure 3.8: Nondimensional velocity magnitude snapshot at $t^* = 1.19$ with point of zero wall shear stress at 73.7°

gradient vanishes. The point of vanishing wall shear originates at the trailing edge of the cylinder and travels quickly upstream to 74.9°. More information on unsteady flow separation may be found in [41] or in [38].

3.5.2   Dynamic Response and Output of Hair at 15°

Here we describe the dynamic response of hair 15 (placed at 15° on the cylinder wall) to the flow over the impulsively started cylinder. For the following results,

Kelvin-Voigt material damping was set to 10^8 Ns/m^2.

The incident flow velocity, u_n, on hair 15 was four orders of magnitude larger than the hair velocity, r_t, so that the relative flow velocity, shown in Figure 3.9, was identical to the incident flow velocity computed from the Navier-Stokes data.
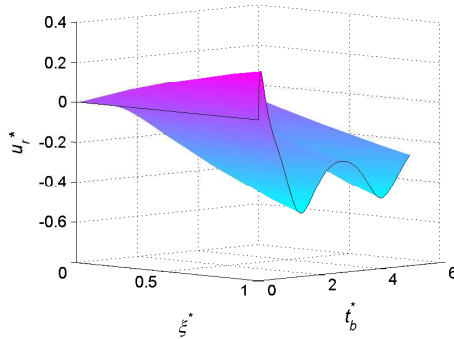
Figure 3.9: Relative flow velocity for hair 15
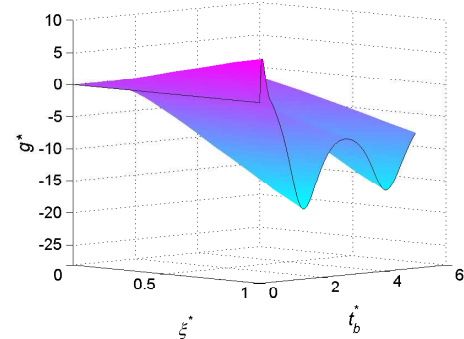
Figure 3.10: Load intensity acting on hair 15

Figure 3.9 shows the initial flow impulse, followed by flow reversal, which indicates the point of zero wall shear stress has moved upstream of 15° on the cylinder wall. Oscillations shown in the reversed flow are a result of the movement of the large clockwise eddy within the flow domain.

The load intensity (Figure 3.10) was in phase with the relative flow velocity (Figure 3.9). This result was expected since $g^* \propto u_r^{*4/3}$, which was obtained with the substitution of equation (3.7) into (3.4). The deflection of hair 15 due to the load intensity (Figure 3.10) is shown in Figure 3.11.

The hair output, M^* (Figure 3.12) followed changes in the tip load intensity in time (Figure 3.10). Since the load intensity was in phase with the relative flow velocity, the moment of hair 15 provided a reasonably time accurate indication of the incident flow velocity direction and magnitude.

Due to the similarity between the load intensity and hair output, it appears that the hair output was dominated by surface forces due to the surrounding viscous
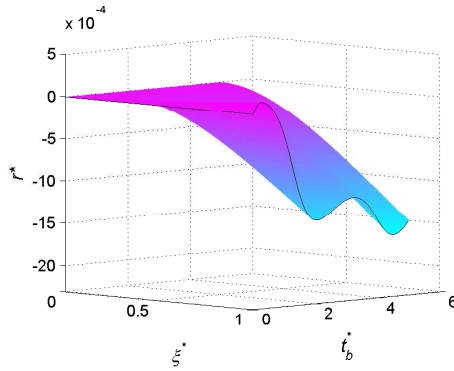
Figure 3.11: Deflection of hair 15
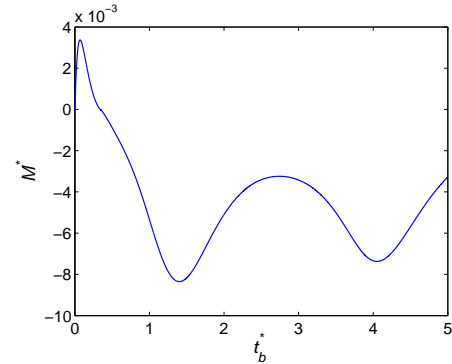
Figure 3.12: Output of hair sensor 15

airflow. However, the material damping, γ, and the modulus of elasticity, E, may also determine the hair dynamics thereby affecting the output through inertial forces present in the hair.

To this end, we asked if changing the rate of relaxation could change the inertial forces in hair 15 enough to significantly affect the hair output. To answer this question, hair 15 was simulated for $\gamma = 10^4$, 10^6, and $10^{10}\,\mathrm{Ns/m^2}$ while holding $E = 10^8\,\mathrm{N/m^2}$ ($\tau = 10^4$, 10^2, $10^{-2}\,\mathrm{s^{-1}}$). Results from the above simulations $\gamma = 10^8\,\mathrm{Ns/m^2}$ ($\tau = 10^0\,\mathrm{s^{-1}}$) were also included in this analysis.

As τ increased from 10^{-2} to $10^4\,\mathrm{s^{-1}}$ the maximum hair deflection increased from 0.01% to 0.23%, as shown in Figure 3.13. Note that for $\tau \geq 10^2$, the hair deflection
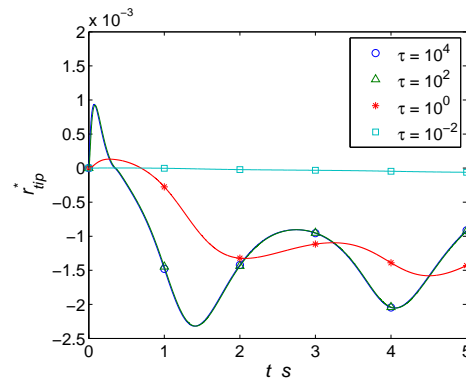
Figure 3.13: Tip deflection of sensor 15 versus time for various τ

converges to a shape similar to the tip load intensity (Figure 3.10), so that it moves in phase with changes in the relative flow velocity.

If the applied load intensity is time dependent, as in our hair/fluid problem, then the dynamic response depends on the relative size of the material time scale, $1/\tau$, and the time scale of the forcing on the hair, further denoted η. For $1/\tau < \eta$, strain in the hair will relax at a higher rate than the load intensity changes in time so that the hair will deflect in phase with changes in the load intensity. In contrast, for $1/\tau > \eta$, the strain from past forces linger in the hair as the load intensity changes. As a result, the hair deflection will move out of sync with the load intensity, being slower to respond to changes in the surrounding viscous flow.

Since the load intensity (Figure 3.10) was in phase with the flow incident on the hair (Figure 3.9), we take the time scale of the load intensity as the inverse of the impulse inlet parameter, $\eta = 1/\lambda = 6.7 \times 10^{-2}\,\mathrm{s}$ (see equation 3.1, Section 3.3). Tip hair deflections (Figure 3.13) for $1/\tau = 10^{-2}\,\mathrm{and}\,10^{-4}\,\mathrm{s}$ $(1/\tau < \eta)$ were in phase with changes in the tip load intensity (Figure 3.10), while hair deflections for $1/\tau = 10^{0}\,\mathrm{and}\,10^{2}\,\mathrm{s}$ showed a longer time periods for strain relaxation and increasingly smaller deflections in time.

Increasing in the rate of relaxation also increased the hair velocity. Still, the largest hair velocity, which occurred during an impulse like response for $1/\tau < \eta$ (Figure 3.14), was three orders of magnitude less than the incident flow velocity.

Despite the different dynamic hair responses above (Figure 3.13 and 3.14), the corresponding hair moments, shown in Figure 3.15, differed by values on the order of 10^{-6} and thus were identical when plotted.

In summary, we have shown that the moment at the base of a hair in unsteady flow separation at Re=500 provided a time accurate indication of the incident flow velocity direction and magnitude. The dynamic response was shown to have neg-
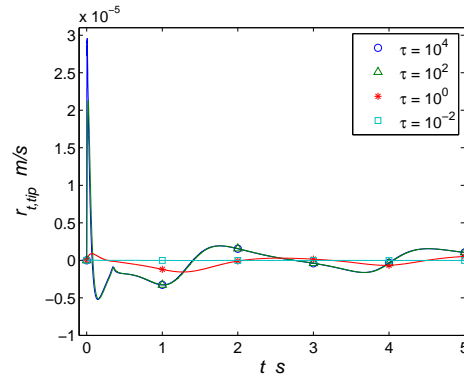
Figure 3.14: Tip velocity of sensor 15 versus time for various τ
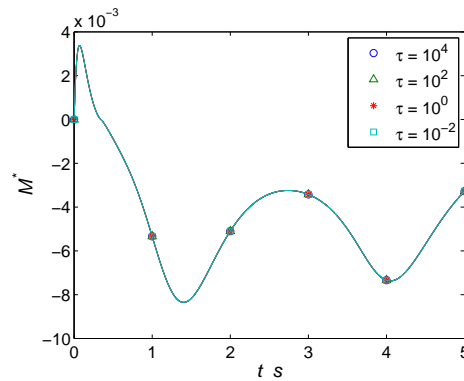
Figure 3.15: Moment output of sensor 15 versus time for various τ

ligible influence on the hair moment, which was dominated by surface forces from the surrounding viscous airflow. Although it remains to be shown, we expect these results will extend to higher Reynolds number flows due to the low Reynolds number environment of the hair receptor described in Section 3.3.

3.5.3 Detection of Unsteady Flow Separation with Hair Array Moments

We now present the set of moments from the complete hair array response to the flow over an impulsively started cylinder simulation, described in Section 3.3.1.

Figure 3.16 is plot of the hair moment, $M^*(t)$, versus hair position and nondimensional time, $t^* = tU/D$. For reference, iso-moment contours are superimposed in
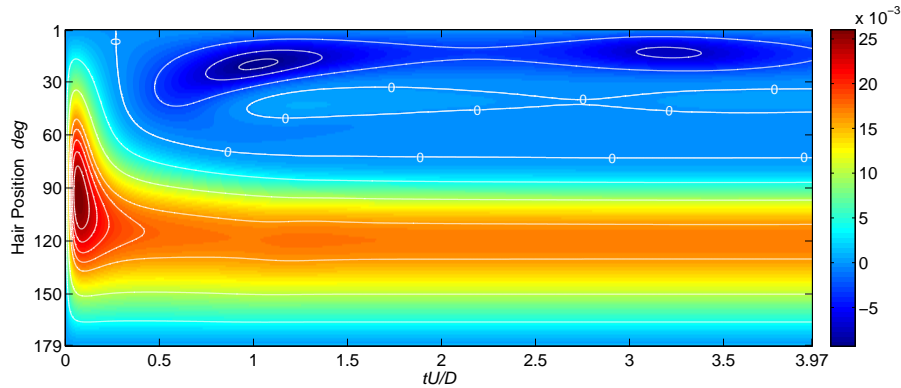
Figure 3.16: Hair array output to flow over an impulsively started cylinder simulation

Figure 3.16 including the zero moment contour.

Figure 3.16, shows the initial flow impulse during which a global maximum moment of 2.60×10^{-1} occurs at $96°$ and $t^* = 0.074$. At $t^* = 0.27$ and $1°$, the zero-moment contour indicates the onset of unsteady flow separation by providing the location of the point of zero wall shear stress, which was observed in the flow at $t^* = 0.25$. From the zero-moment contour, the location of zero wall shear stress quickly moves upstream to $72°$, a phenomena consistent with past numerical studies of flow over an impulsively started cylinder [42].

Within the separated boundary layer, a global minimum of -9.3×10^{-3} at $t^* = 1.02$ at hair 20 occurs due to the growth of the large clockwise eddy. At $t^* = 0.97$ and hair 45, the beginning of another zero-moment contour is observed that grows to contain positive moments, indicating forward flow spanning its boundaries. In fact, this response is due to a small counterclockwise eddy upstream of the larger clockwise eddy. The counterclockwise eddy is paired with a third clockwise eddy represented in the array output between the upstream boundary of the zero valued contour of the counterclockwise eddy and the zero wall shear stress contour, where hair outputs are negative. This scenario is illustrated in Figure 3.17 with a vector velocity plot spanning $33°$ to $74°$ at $t^* = 1.50$.
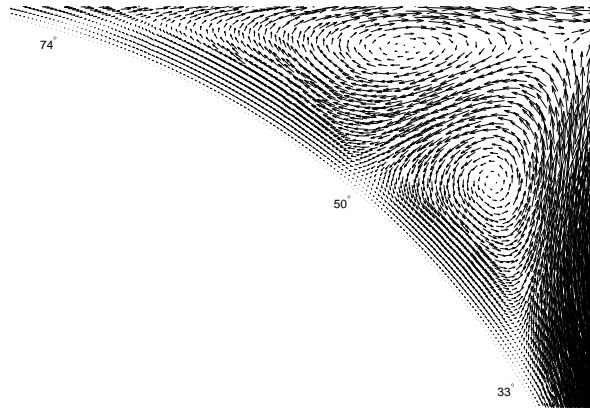
Figure 3.17: Vector velocity at $t^* = 1.50$ near the cylinder wall showing the counter rotating eddies detected by the hair array between 33° and 74°

For $t^* > 1.50$, the span of the zero-moment contour due to the counterclockwise eddy is shown to contract, then grow again. Concurrently downstream, the values and span of the negative moments due to the large clockwise eddy are shown to vary. These fluctuations are an outcome of both the growth and movement of the near wall eddies within the flow domain. Due to the apparent sensitivity of the hair moment to near wall eddies, we anticipate that the moments from hair arrays are also a means to detect vortex shedding and its periodicity.

3.6   Summary

Biologists hypothesize that the thousands of hairs scattered across the bat wing are a sensing network for detecting airflow patterns and part of a biological feedback flow control loop. In this work, we investigated the hair array as a means for flow detection by simulating their output to the flow over an impulsively started cylinder.

Observations of a single hair response to the flow showed that its output provided a time accurate indication of the incident flow velocity and direction, including flow reversal due to separation. A brief parameter investigation showed surface forces from

the external airflow dominated the inertial forces of the hair.

An array of 179 hairs placed on the cylinder wall revealed features of the flow impulse and subsequent unsteady flow separation with impressive accuracy and detail. Observations between the output of the hair array and the flow were in agreement with the onset and span of reversed flow, the movement of the point of zero wall shear stress, the movement of eddies away from the wall, and the formation of a small counter-rotating pair of eddies upstream of the larger clockwise eddy. These results support the utility of artificial hair sensor arrays for flow controller designs in the MAV, and are consistent with the hypothesis that bats use hair receptor arrays to detect unsteady flow patterns.

Future work will focus on the sensitivity hair receptors in boundary layer flows. Through an investigation with the boundary layer, we aim to determine the best hair geometry (e.g., profile, length) and placement for boundary layer detection on an aircraft wing.

BOUNDARY LAYER DETECTION WITH HAIR SENSORS

B. T. Dickinson

4.1 Abstract

Biologists have shown that bats possess hair sensors scattered over their wing surfaces. It is hypothesized that the hair sensors provide airflow feedback over the bat wings for enhanced stability and maneuverability during flight. Here, we consider hair-like structures, such as those found on the bat wings, as boundary layer transducers. A quasi-steady model that relates the flow velocity profile incident on the hair to the resultant moment and shear force at the hair base is developed. The hair length relative to the boundary layer momentum thickness that maximizes resultant moment and shear-force sensitivity to boundary layer shape is determined for hairs with uniform and linearly tapered cross-section. Resultant moment and shear-force sensitivity is shown to be highly dependent on hair length. Hairs that linearly taper to a point are shown to provide more sensitivity over a larger range of flow conditions than hairs of uniform cross-section. On an order of magnitude basis, the computed optimal hair lengths are in exact agreement with the range of biological hair sensor lengths measured on individual bat species. These results support the hypothesis that bats use hair sensors for boundary layer detection and provide geometric guidelines for artificial hair sensor design and integration into micro-air-vehicles.

4.2 Introduction

Recent histological studies of bat wings have found distributed arrays of hair receptors (Figure 4.1) on the dorsal and ventral wing surfaces [1]. The hair receptors are smaller than pelagial hair and found growing from domes that contain touch sensitive cells [2].
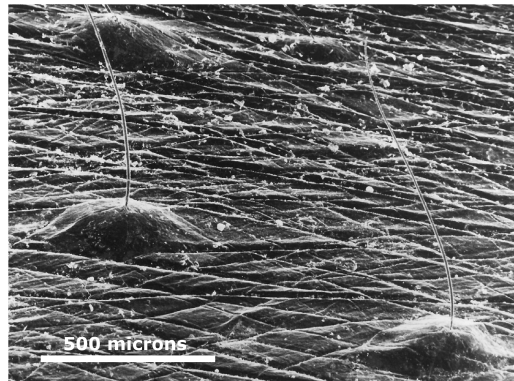
Figure 4.1: Scanning electron micrograph of hair cells on the wing of the grey-headed flying-fox (Reproduced by permission of CSIRO PUBLISHING, from the Australian Journal of Zoology vol. 42(2):215-231 (GV Crowley and LS Hall). Copyright CSIRO 1994. http://www.publish.csiro.au/nid/91/issue/2300.htm)

Forces on the hair from the airflow environment create afferent bioelectrical signals in the hair dome; however, how this information is used and the specific flow features or quantities being detected is unknown. Inspired by the hair receptor array on bat wings, here we investigate hair-like structures for the detection of boundary layer flows.

The detection of the spatial development or evolution of boundary layer flows over aircraft wings could be used to maintain a laminar attached boundary layer flows and reduce skin friction drag. For these purposes, linear optimal model-based control methodologies have been applied to boundary layer flows with promising results [43, 44]. In these (and many other) studies the focus is on control design and the estimation of the boundary layer from limited pressure and shear-stress information at the wall.

In the real application of flow control and estimator designs, pressure and wall shear-stress information is provided by a suite of surface mounted sensors. A hair sensor array is one potential suite of sensors for wall shear-stress measurement through the detection of boundary layer shape. The effective integration of hair sensors (or

other sensor types) into flow control and estimator designs requires an understanding of the interaction of the sensor with the flow and an accurate mathematical model that relates flow state information (e.g. velocity field) to sensor output. Sensor placement and the number of sensors necessary for acceptable estimator and controller performance is also a design issue and generally an open question. Still, before hair-like structures may be integrated as sensors in flow control and estimator designs, boundary layer detection leads to geometric considerations of the hair for optimal sensor performance.

In this work, our goal is to determine the hair length that provides the maximum output sensitivity to changes in boundary layer shape. Based on hair and flow time scales, we develop a quasi-steady hair sensor model relating the incident flow velocity (the sensor input) to the resultant moment and shear force at the base of the hair (sensor output). Hair output was computed for a set of boundary layer flows modeled by the Falkner-Skan equation. The hair lengths relative to the boundary layer thickness that provided the maximum output sensitivity were determined for hairs with uniform and linearly tapered cross section.

For both hair profiles, hair output sensitivity is highly dependent on hair length with the optimal hair lengths for maximum output sensitivity ranging from 43.0% to 115% of δ_{99}, depending on the hair shape and output quantity (moment or shear force). The optimal lengths of linearly tapered hairs were approximately 10% longer than hairs with uniform cross section. Additionally, linearly tapered hairs provided a slightly increased output sensitivity over a larger range of boundary layer thicknesses than hairs with uniform cross section.

By estimating the range of boundary layer thicknesses over bat wings during flight, an approximate range of optimal hair lengths for boundary layer detection over the bat wing was determined. On an order of magnitude basis, the ranges of measured

hair lengths on three different bat species were in exact agreement with the ranges of computed values.

The following section contains a description of the flow environment surrounding the hair and presents our approach to the development of a quasi-steady hair model. In Section 4.4 the hair output is reported for various hair lengths and boundary layer shapes and the optimal hair length for maximum output sensitivity is determined. We conclude with a summary of our approach and findings.

4.3   Hair Sensor Model

Although electrical signals are the form of the actual output of both biological and artificial hair sensors, we take the hair sensor output as the resultant moment and shear force at the base of the hair. This choice of output is made with the assumption that the resultant moment and shear force is related to the electrical output signal with additional modeling of the biological mechanism or MEMS devices.

The goal in modeling the hair receptor is to develop a relationship between the nearby flow that applies surface forces to the hair, further referred to as the sensor input (Figure 4.2a), and the resultant shear force and moment at the base of the hair, further together referred to as the hair output (Figure 4.2b).

We begin our development of a mathematical hair sensor model with a conceptual discussion of the forces in the airflow over a hair. Let the Reynolds number for flow normal to the hair longitudinal axis (the axis normal to the hair cross section) be defined as

$$\mathrm{Re}_0 = \frac{U \, d_0}{\nu} \tag{4.1}$$

where U and d_0 are the characteristic flow velocity and characteristic hair diameter, respectively. Setting $U \sim 1\mathrm{m/s}$ as a characteristic speed of bat and MAV flight,
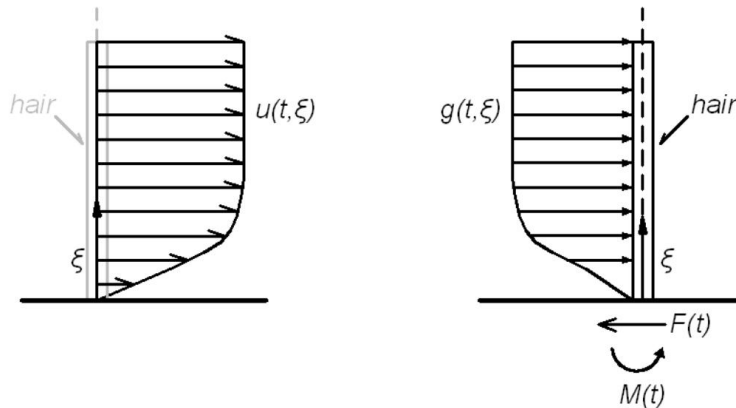
Figure 4.2: Nonuniform flow velocity profile incident on hair receptor (*left*) and corresponding free body diagram of hair (*right*)

(the symbol $\sim$ is used here to mean *on the order of magnitude*) and $d_0 \sim 10^{-5}$m, a characteristic diameter of bat hair sensors, gives $\text{Re}_0 \sim 1$. Although not quite a Stokes flow environment, $\text{Re}_0 \sim 1$ illustrates the importance of viscous forces from the airflow over the hair. Previous studies also found that hair motion is driven by surface forces (see [34, 37] or [35] and the references therein).

Relative hair motion due to deflection with or against the flow velocity hair may also affect the surface forces acting on the hair. To understand the importance of relative hair motion on surface forces we compared the hair and flow time scales. The time scale of a hair's dynamic response to an applied stress may be quantified with the ratio of the coefficient of material damping, γ, to the modulus of elasticity, E [39]. Although experiments to determine these material properties of bat hairs have yet to be performed, mammalian hair is composed of keratin for which many mechanical and dynamic properties are known. For example, the dynamic time scale of keratin wool fibers ranges from $\sim 10^1$ to $\sim 10^5$ seconds, depending on the relative humidity of air [45]. Here, we use this range of time scales as an estimate for bat hair sensor dynamics.

As a time scale of flow over the hair we take the ratio of the characteristic hair

diameter, d_0, to the characteristic flow velocity U, d_0/U. Using the above characteristic values for d_0 and U, the micro-scale hair diameter leads to time scales of $\sim 10^{-6}$ seconds. Clearly, for keratin and potentially a wide range of viscoelastic materials,

$$\frac{\gamma}{E} >> \frac{d_0}{U}.$$

To this end, the hair is effectively motionless from the perspective of the flow and will exhibit quasi-steady behavior.

Given the statically determinate situation of the hair (Figure 4.2) and making the assumption of quasi-steady behavior leads to the following expressions for resultant moment and shear force

$$M(t) = \int_0^\ell g(t, \xi)\, \xi\, d\xi \qquad (4.2)$$

and

$$F(t) = \int_0^\ell g(t, \xi)\, d\xi. \qquad (4.3)$$

where $g(t, \xi)$ is the instantaneous load intensity that acts normal to the longitudinal axis having units of force per unit length.

For hairs with circular cross section, we approximate the load intensity at any longitudinal position, ξ, along the hair as

$$g(t,\xi) = \frac{1}{2}\, C_d(\mathrm{Re}_\xi)\, \rho\, d(\xi)\, u(t,\xi)^2 \qquad (4.4)$$

for $0 \leq \xi \leq \ell$ where ℓ is hair length, ρ is the fluid density, d is the hair diameter, u is the flow velocity incident on the longitudinal axis, and C_d is the drag coefficient for an infinite circular cylinder in cross-flow. Due to the nonuniform boundary layer profile and a potentially nonuniform hair diameter, the drag coefficient, C_d, is determined

as a function of the local Reynolds number,

$$\text{Re}_\xi = \frac{u(t, \xi)\, d(\xi)}{\nu},\tag{4.5}$$

with a least squares fit to empirical data for the drag coefficient of infinite circular cylinders in crossflow over $10^{-1} \leq \text{Re}_\xi \leq 10^1$ found in [46] and routinely contained in most fundamental texts on fluid mechanics. Close agreement with experimental data was observed with the following linear logarithmic expression

$$\log C_d \approx -\frac{2}{3} \log \text{Re}_\xi + \frac{5}{2}.\tag{4.6}$$

Note that the use of the drag coefficient in the expression for the load intensity (4.4) does not account for flow phenomena due to its free end or the surface where the hair is mounted. Although end effects will be present, we anticipate their influence on the surface forces acting on the hair will be negligible due to the low Reynolds number environment ($\text{Re}_0 \sim 1$ or less).

When the expression for load intensity (4.4) is substituted into the equations for resultant moment (4.2) and shear (4.3) we obtain

$$M(t) = \int_0^\ell \frac{1}{2} C_d(\text{Re}_\xi)\, \rho\, d(\xi)\, u(t, \xi)^2\, \xi\, d\xi\tag{4.7}$$

and

$$F(t) = \int_0^\ell \frac{1}{2} C_d(\text{Re}_\xi)\, \rho\, d(\xi)\, u(t, \xi)^2\, d\xi.\tag{4.8}$$

Equations (4.7) and (4.8) relate the velocity profile of a viscous incompressible flow normal to the longitudinal axis of a hair-like structure having circular cross-section to the mechanical response at its base. In the following section we proceed with a

nondimensionalization of equations (4.7) and (4.8) to length and velocity scales of the boundary layer.

4.3.1 Nondimensional Form of Hair Model

For analysis within the context of boundary layer flows, we now recast equations (4.7) and (4.8) with the following nondimensional variables

$$d^* = \frac{d}{d_0}, \quad \xi^* = \frac{\xi}{\delta_2}, \quad \ell^* = \frac{\ell}{\delta_2}, \quad u^* = \frac{u}{U}, \tag{4.9}$$

where d_0 is a characteristic hair diameter (taken here as the base diameter $d(\xi = 0) = d_0$), δ_2 is the boundary layer momentum thickness, and U is the external flow velocity.

The application of (4.9) to the resultant moment (4.7) results in an equivalent expression that is the product of a nondimensional coefficient of moment,

$$C_m = \frac{1}{\ell^{*2}} \int_0^{\ell^*} C_d(u^*, d^*, \mathrm{Re}_0)\, d^*\, u^{*2}\, \xi^*\, d\xi^* \tag{4.10}$$

the dynamic pressure, $Q = \frac{1}{2}\rho U^2$, the frontal area, $A = d_0\,\ell$, and the characteristic length, ℓ, as

$$M(t) = C_m\, Q\, A\, \ell. \tag{4.11}$$

With a similar application of the nondimensional scales in (4.9) to the resultant shear force (4.8) we obtain the product of a nondimensional coefficient of shear force,

$$C_s = \frac{1}{\ell^*} \int_0^{\ell^*} C_d(u^*, d^*, \mathrm{Re}_0)\, d^*\, u^{*2}\, d\xi^*, \tag{4.12}$$

the dynamic pressure, Q, and frontal area, A, as

$$F(t) = C_s\, Q\, A. \tag{4.13}$$

The coefficients of moment (4.10) and shear force (4.12) are primarily a function of the nondimensional variables u^*, d^* and ℓ^* and are secondary functions of the reference Reynolds number, Re_0 (4.1). The dependence on Re_0 is obtained by applying (4.9) to local Reynolds number (4.5) as $\mathrm{Re}_\xi = u^*\, d^*\, \mathrm{Re}_0$.

4.3.2 Boundary Layer Model

Computing hair output sensitivity requires an adequate description of changes in boundary layer shape. Here, we chose the Falkner-Skan equation which describes boundary layer flows over a wedge (accelerated flows), corner (retarded flows), and flat plate (Blasius flow). The Falker-Skan equation is obtained from Prandtl's boundary layer equations with the assumption of self-similar solutions and is written as

$$
\begin{aligned}
f''' + f\, f'' + \beta\, (1 - f'^2) &= 0, \\
f(0) = f'(0) &= 0, \\
f'(\eta \to \infty), &= 1
\end{aligned}
\tag{4.14}
$$

where $f = f(\eta)$ is a similarity variable, $f' = u^* = u/U$, $\eta = y/\delta$ is a dimensionless wall normal coordinate and U is the outer flow. The boundary layer thickness measure, δ, is

$$\delta = \sqrt{\frac{2}{m+1}\frac{\nu\, x}{U}} \tag{4.15}$$

where $m = \beta/(2 - \beta)$ and the parameter β determines the corresponding geometry of the flow (i.e. plate, corner, wedge, etc.).

Since no analytical solution of (4.14) is known, solutions of the Falkner-Skan equation must be approximated numerically. Here, we used a second-order accurate central-difference scheme known as the Keller box-method [47]. Figure 4.3 contains grid independent boundary layer profiles from the solution of (4.14) for β ranging from $\beta = -0.199$ (separation over a corner) to $\beta = 1.0$ (flow to a plane stagnation point).
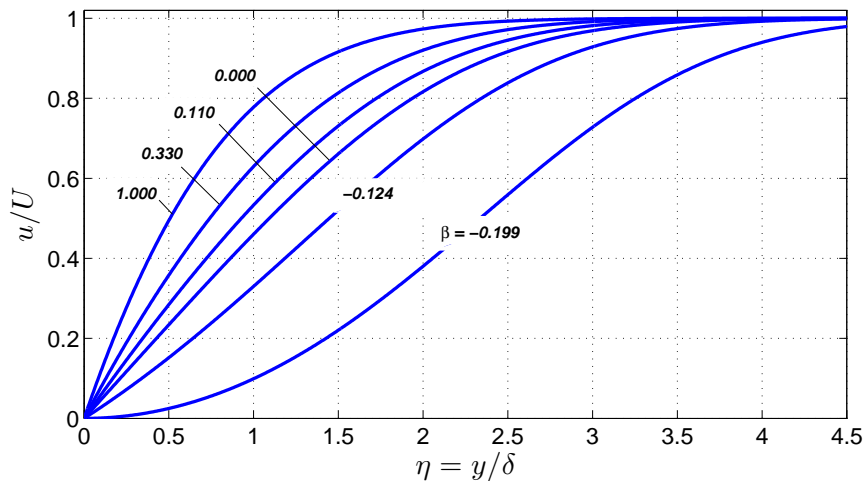
Figure 4.3: Solutions of the Falkner-Skan equation ranging from separation ($\beta = -0.199$) to plane stagnation ($\beta = 1.0$)

Boundary layer shapes, such as those shown in Figure 4.3, are further quantified herein with the Hartree shape factor,

$$H = \frac{\delta_1}{\delta_2},$$

where δ_1 is displacement thickness,

$$\delta_1 = \int_0^\infty \left(1 - \frac{u}{U}\right) d\eta,$$

and δ_2 is the momentum thickness,

$$\delta_2 = \int_0^\infty \frac{u}{U}\left(1 - \frac{u}{U}\right) d\eta.$$

In terms of the Hartree shape factor, separation occurs when $H=4.029$, $H=2.591$ corresponds to Blasius flow (flow over a flat plate), and $H=2.216$ indicates flow to a plane stagnation point (Heimenz flow). For more information on the Falker-Skan equations and Hartree profiles see Schlichting and Gersten [38].

4.4 The Optimal Hair Length for Boundary Layer Detection

Any portion of a hair protruding from the boundary layer will have a corresponding portion of its output represented by the external flow. Hairs that extend too far into the external flow will be insensitive to changes in the boundary layer. Thus, for maximum output sensitivity to changes in boundary layer shape we propose that the hair length be limited by a measure of the local boundary layer thickness.

We search for the hair length of largest output sensitivity over $0.01 \leq \ell^* \leq 6$ and boundary layer shapes over $2.216 \leq H \leq 4.029$. To specifically examine sensitivity to boundary layer shape, hair moment (4.11) is nondimensionalized by the reference moment, $Q\,A\,\ell$, and normalized by the dependence of C_m on the external flow, U, through Re_0 leading to the following nondimensional expression

$$M^* = C_m\,\mathrm{Re}_0^{2/3} = \frac{1}{\ell^{*2}} \int_0^{\ell^*} d^{*1/3}\,u^{*4/3}\,\xi^*\,d\xi^*. \tag{4.16}$$

Similarly, the resultant shear force (4.13) is nondimensionalized by the reference force,

$Q A$, and normalized by its dependence on U to give

$$F^* = C_s \, \mathrm{Re}_0^{2/3} = \frac{1}{\ell^*} \int_0^{\ell^*} d^{*1/3} \, u^{*4/3} \, d\xi^*. \tag{4.17}$$

Equations (4.16) and (4.17) are general nondimensional expressions for laminar bound-ary layer flows. Note that for the direct application of (4.16) and (4.17) to Falkner-Skan solutions, we may rescale hair length and wall normal distance by δ (4.15), a specific measure of boundary layer thickness for Falkner-Skan flow, to obtain the following expressions that are equivalent to equations (4.16) and (4.17) above,

$$M^* = \left(\frac{\delta}{\ell}\right)^2 \int_0^{\ell/\delta} d^{*1/3} \, f'^{4/3} \eta \, d\eta \tag{4.18}$$

and

$$F^* = \left(\frac{\delta}{\ell}\right) \int_0^{\ell/\delta} d^{*1/3} \, f'^{4/3} \, d\eta. \tag{4.19}$$

Equations (4.18) and (4.19) are used in the following sections to compute the hair output and sensitivity.

4.4.1 Hairs with Uniform Cross-Section

This section contains the output and sensitivity of hairs with a uniform cross-section of $d = d_0 = 10 \, \mu$m. Figures 4.4 and 4.5 are contour plots of M^* and F^* versus $\ell^* = \ell/\delta_2$ and H, respectively. The lines in Figures 4.4 and 4.5 represent iso-moment and iso-shear contours, which trace paths of increasing ℓ^* as H increases from 2.216 to 4.029. The direction of the iso-output contours is an outcome of the flow changing from a situation where motion in the downstream direction is accelerated by a decreasing pressure gradient, to one where downstream motion is impeded by an increasing
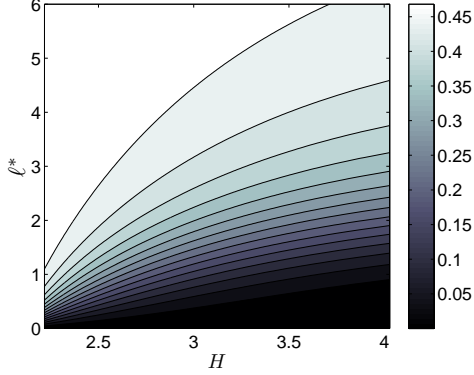
Figure 4.4: M^* as a function of ℓ^* and H for a hair sensor with uniform cross section
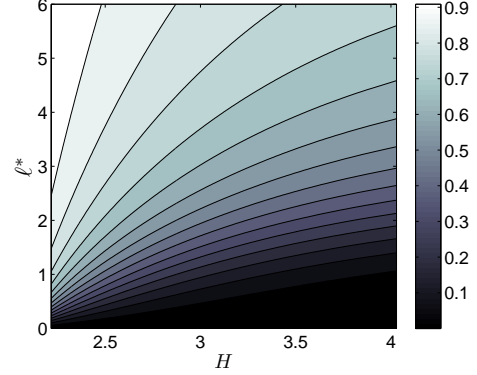
Figure 4.5: F^* as a function of ℓ^* and H for a hair sensor with uniform cross section

pressure gradient. For a hair mounted within the boundary layer, an increase in H corresponds to a decrease in nondimensional incident flow velocity, u/U (see Figure 4.3). It follows that the iso-output contours follow paths of increasing length to supplement the output loss as H increases.

For all hair lengths, maximum outputs occur for the most accelerated flows (Hiemenz flow, $H = 2.216$). As the flow decelerates (H increases from $H = 2.216$), all hair outputs monotonically decrease to minimum values at $H = 4.029$. This monotonic behavior leads to a convenient quantification of hair output sensitivity: the values spanned by M^* and F^* over $2.216 \leq H \leq 4.029$ or

$$S_{M^*} = M^*_{max} - M^*_{min} \tag{4.20}$$

and

$$S_{F^*} = F^*_{max} - F^*_{min}. \tag{4.21}$$

When the above sensitivities, (4.20) and (4.21) are plotted against ℓ^* (Figure 4.6) distinct values of maximum sensitivities for moment and shear occur at $\ell^* = 0.93$

and $\ell^* = 1.17$, respectively. We shall further refer to lengths of maximum sensitivity
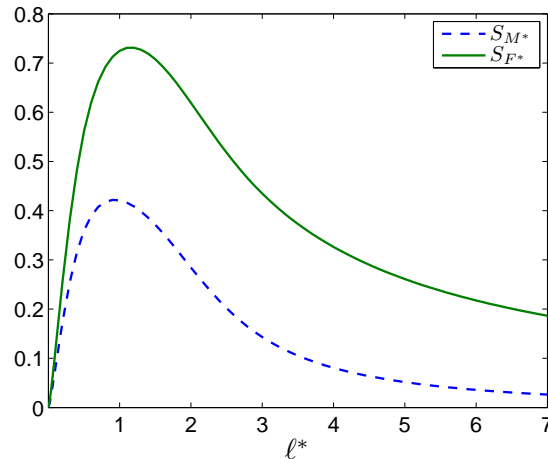
Figure 4.6: Sensitivity of hair, S_{M^*} and S_{F^*}, with a uniform diameter as a function of ℓ^*

as *optimal* and denote their values for output moment and shear with the subscript $(\cdot)_{M^*}$ and $(\cdot)^*_F$, respectively.

Nondimensional hair lengths scaled by the Falkner-Skan boundary layer thickness, δ (4.15), result in optimal values of $(\ell/\delta)_{M^*} = 2.07$ and $(\ell/\delta)_{F^*} = 2.41$. As H decreases from $H = 4.029$ to 2.216 the optimal hair lengths increase from 43.0% to 86.3% of δ_{99} for moment and from 50.1% to 100% of δ_{99} for shear force.

Finally, we note that as the relative hair lengths moves from their optimal values in Figure 4.6, output sensitivity sharply decreases, indicating that hair length is a critical geometric parameter for the detection of boundary layer profiles.

4.4.2 Hairs with Linearly Tapered Cross-Section

Bat hair receptors have nonuniform cross-sections that are thickest at their base and taper to smaller diameters toward the tip. To this end, the above computations were also performed for hairs with a constant base diameter of 1×10^{-5}m (also taken as

the reference diameter d_0) that linearly taper to a point.

Hair outputs versus length ℓ^* and Hartree profile H^* showed similar trends to hairs with uniform cross-section (Figures 4.7 and 4.8). Again, the output sensitivities
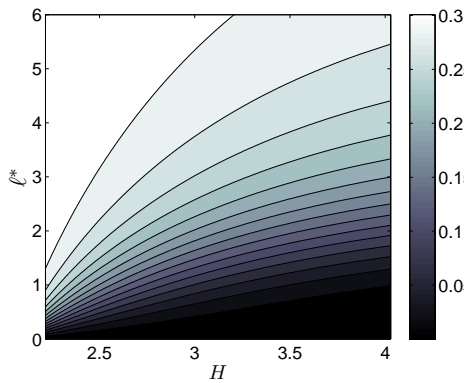
Figure 4.7: M^* as a function of ℓ^* and H for a hair sensor with tapered cross-section
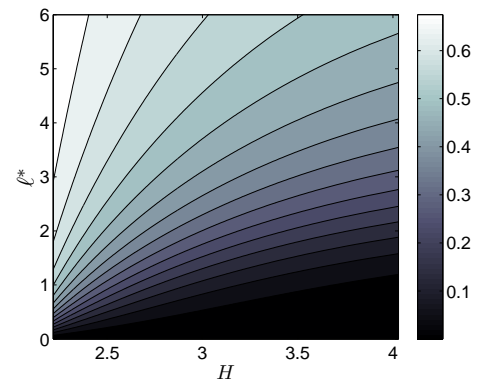
Figure 4.8: F^* as a function of ℓ^* and H for a hair sensor with tapered cross-section

(4.20) and (4.21) showed distinct optimal hair lengths (Figure 4.9) with points of maximum moment and shear sensitivity of $\ell^*_{M^*} = 1.05$ and $\ell^*_{F^*} = 1.34$. In terms
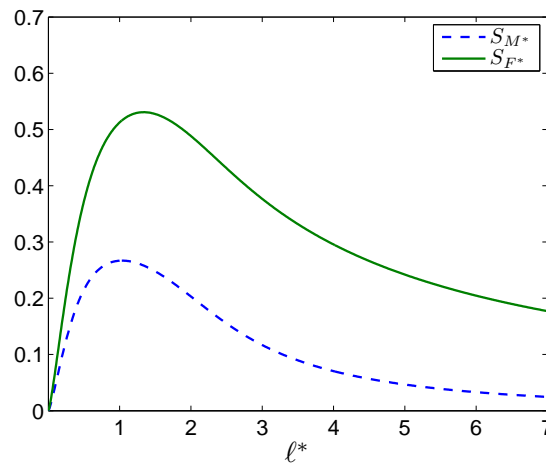
Figure 4.9: Sensitivity of hair, S_{M^*} and S_{F^*}, with a linearly tapered diameter as a function of ℓ^*

of the Falkner-Skan boundary layer thickness, δ, the optimal hair lengths occur at

$(\ell/\delta)_{M^*} = 2.27$ and $(\ell/\delta)_{F^*} = 2.75$. As H decreases from $H = 4.029$ to 2.216 the optimal hair lengths increase from 47.2% to 94.6% of δ_{99} for moment and from 57.2% to 115% of δ_{99} for shear force.

The 15% extension of the optimal tapered hair length past δ_{99} for $H = 2.216$ is not completely unexpected. Although increasing a tapered hair length beyond the boundary layer thickness creates an output contribution from the external flow, an increase in the diameter subject to the boundary layer profile also occurs (note that this cannot be said for hairs with uniform cross-section). Thus, for a certain length beyond the boundary layer, loss of output sensitivity from the contributions by the external flow is outweighed by the advantage of an increase in hair diameter within the boundary layer.

Close comparison Figure 4.9 with Figure 4.6 also shows slightly less penalty in output sensitivity as hair lengths move away from their optimal points. To this end, it appears that a tapered hair profile may be a means of preserving sensor sensitivity as flow conditions change near the hair.

The results in Sections 4.4.1 and 4.4.2 provide insight into artificial hair sensor design and integration into micro-air-vehicles. For the detection of the boundary layer (as opposed to the external flow) hair length should be chosen based on *a priori* knowledge of the boundary layer thickness. The optimal values of ℓ^* determined herein serve as guidelines for ensuring hair output sensitivity. These values are summarized in the first two columns of Table 4.1 below. Included in the third and fourth

Table 4.1: Summary of optimal relative hair lengths determined herein for hairs with uniform and linearly tapered cross-section

Hair Shape	$(\ell/\delta_2)_{M^*}$	$(\ell/\delta_2)_{F^*}$	$(\ell/\delta)_{M^*}$	$(\ell/\delta)_{F^*}$	$(\ell/\delta_{99})_{M^*}$	$(\ell/\delta_{99})_{F^*}$
Uniform	0.93	1.17	2.07	2.41	0.430-0.863	0.501-1.00
Tapered	1.05	1.34	2.27	2.75	0.472-0.946	0.572-1.15

columns of Table 4.1 are the optimal hair lengths with respect to δ (4.15). However, because δ depends on m and x, the meaning of these values is limited to self-similar flows where these parameters have meaning. Finally, the ranges of hair length relative to δ_{99} for $2.216 \leq H \leq 4.029$ are listed in the last two columns.

4.4.3   Comparison of Optimal Hair Lengths with Biological Data

We now estimate the range of optimal hair lengths over the bat wing and compare these results to the range of hair receptor lengths measured on three different bat species. For each bat, the range of optimal hair lengths are computed by estimating the range of boundary layer thicknesses over the wing given flight-speed and chord-length data. The range of boundary layer thicknesses over the bat wing is estimated with the range of boundary layer thicknesses of Falkner-Skan solutions having surface lengths, L, equal to bat wing average chord-lengths and boundary layer shapes over $2.216 \leq H \leq 4.029$ and at equal Reynolds numbers.

A Reynolds number for the forward flapping flight of the bats [10] is

$$\mathrm{Re}_b = \frac{V_f\, L_c}{\nu}, \tag{4.22}$$

where V_f is the forward flight speed and L_c is the mean wing chord-length, defined as the wing area divided by the wing span. For the Falkner-Skan flow we use the following Reynolds number

$$\mathrm{Re} = \frac{V\, L}{\nu}, \tag{4.23}$$

where V is a reference velocity taken as the external flow velocity evaluated at the trailing edge $(x = L)$ of the no slip surface and L is the streamwise surface length. We then take $V = V_f$ and $L = L_c$ so that $\mathrm{Re}_b = \mathrm{Re}$.

Recall that the optimal hair lengths relative to δ, for linearly tapered hairs were computed as $(\ell/\delta)_{M*} = 2.27$ and $(\ell/\delta)_{F*} = 2.75$, as listed in Table 4.1. With equation (4.15) for δ and V_f and L_c substituted for V and L, the dimensional optimal hair lengths are evaluated as

$$\ell_{o,M} = 2.27\sqrt{\frac{2}{m+1}\frac{\nu\,x}{U}} \quad \text{and} \quad \ell_{o,F} = 2.75\sqrt{\frac{2}{m+1}\frac{\nu\,x}{U}}, \tag{4.24}$$

respectively, where $U = V_f\,(x/L_c)^m$ and $m = \beta/(2-\beta)$.

The bat species, their range of forward flight speeds, values of their mean wing chord-lengths, and available data for their hair receptor lengths are listed in the first four respective columns of Table 4.2. The fifth column contains the range of

Table 4.2: Measured bat wing hair receptor lengths and optimal hair lengths computed from bat wing and flight measurements

Species	Air Speed $(\mathrm{m\,s^{-1}})$	Average Wing Chord (m)	Measured Hair Length (μm)	Computed Hair Length (μm)
Pteropus poliocephalus	4-8.6 [48] (enclosed)	0.151 [49]	4000 (max observed [1])	100-3100
Glossophaga soricina	2.7-7.8 [50]	0.079 [51]	150-1000[1]	100-2600
Eptesicus fuscus	3.6-9.2 [36]	0.102	100-2000[1]	100-2600

optimal hair lengths for both moment and shear outputs for $-0.199 \leq \beta \leq 1.0$, $V_{f,min} \leq V_f \leq V_{f,max}$, and $0.01\,L_c \leq x \leq 0.99\,L_c$. On an order of magnitude basis, the range of computed hair lengths are in exact agreement with the range of measured values for each bat. Considering that bat wing hair receptors are distinctly smaller than pelagial hair, the agreement between computed and measured hair lengths is at the most compelling evidence, and at the least contributing evidence to the idea that

---

[1]Data courtesy of The Auditory Neuroethology Laboratory at The University of Maryland

bats use hair receptors to detect boundary layer flows.

Note that the dimensional optimal hair lengths (4.24) is a function of boundary layer shape (represented through β), flight speed V_f, and hair position on the wing. While flight speed and boundary layer shape can vary during flight, hair position on the wing remains constant. Thus, for a given position on the wing the optimal hair length for both biological and man made flyers may be determined based on *a priori* knowledge of the boundary layer flow.

The detection of boundary layer flows with multiple sensors located at different locations leads to a distribution hairs with varying lengths over the lift surface. The equations for dimensional hair length in Falkner-Skan flows provide an expression for length distribution, $\ell \sim x^{1/2}$. Furthermore, the hair sensor length and distribution for any aircraft where flight performance relies on attached boundary layer flows could be determined with knowledge of the momentum thickness over the wing. This information is presently available through numerous computer programs, such as the XFOIL software [52], and through existing data in the literature.

The actual three-dimensional low-Reynolds number flows ($\mathrm{Re}_f \lesssim 10^5$) over bat wings during flapping flight exhibits other aerodynamically important flow phenomena that are not boundary layers. One such phenomena is the leading edge vortex which has been identified as a lift enhancement mechanism (see [10] and the references therein). Near the bat wing leading edge hair lengths may not correspond to the attached boundary layer thicknesses. Although attached laminar boundary layer flows will surely be present at times during bat flight, determining the hair lengths that should be distributed over the bat wings for regions of non-boundary layer flows may require a separate analysis of hair sensitivity for these particular flows.

4.5 Summary

The stability and maneuverability of low-Reynolds number flyers may be enhanced with the detection of boundary layer flows over its lift surfaces. Hair sensor arrays are one potential means for boundary layer detection. In this work, we studied the optimal length of hair sensors for the detection of boundary layer flows. By considering disparate time scales between the hair dynamics and air flow environment, a quasi-steady model relating the boundary layer shape to the resultant moment and shear force at the base of the hair was developed. The hair model was nondimensionalized using momentum thickness as a length scale and the resultant moment and shear force at the base of the hair (output) was computed in Falkner-Skan boundary layer flow. Based on the resulting hair sensor output maps, hair sensitivity was quantified as the total output range for moment and shear as the boundary layer profile changed from wall stagnation ($H = 2.216$) to flow separation ($H = 4.029$).

When sensitivity was plotted against hair length, distinct lengths of maximum sensitivity (optimal lengths) were observed. Hair length was also shown to be a critical design parameter, as both hair shapes experienced a sharp decay in output sensitivity as length moved away from the optimal values. However, the linearly tapered hair showed slightly less penalty in output sensitivity for suboptimal lengths.

Finally, the boundary layer thickness over a bat wing was approximated with Falkner-Skan flow using physical and flight data of bats. On an order of magnitude basis, the range of optimal hair lengths computed from the analysis herein was in exact agreement with the range of measured hair receptor lengths on bat wings ($\sim 100 - 1000\,\mu m$). This result supports the hypothesis that bats uses hair receptors for boundary layer detection.

Future work will focus on determining the optimal hair shape for boundary layer

detection. Additionally, the optimal placement and density of a hair sensors for various low-Reynolds number flows of aerodynamic importance should be studied for their effective integration into micro-air-vehicle control system designs.

Acknowledgments

A SNAPSHOT ALGORITHM FOR LINEAR FEEDBACK FLOW CONTROL DESIGN

B. T. Dickinson,   B. A. Batten   J. R. Singler,

5.1 Abstract

The control of fluid flows has many applications. For micro air vehicles, integrated flow control designs could enhance flight stability by mitigating the effect of destabilizing air flows in their low Reynolds number regimes. However, computing model based feedback control designs can be challenging due to high dimensional discretized flow models. In this work, we investigate the use of a snapshot algorithm proposed in Ref. [14] to approximate the feedback gain operator for a linear incompressible unsteady flow problem on a bounded domain. The main component of the algorithm is obtaining solution snapshots of certain linear flow problems. Numerical results for the example flow problem show convergence of the feedback gains.

5.2 Introduction

Controlling fluid flows has many potential applications. For example, robust feedback control of the air flow around micro air vehicles could lead to enhanced flight performance, stability, and maneuverability. Recent research has shown that a linear feedback controller (or a nonlinear extension thereof) has the potential to delay or even eliminate the onset of turbulence (e.g., see Refs. [53, 54, 55, 56, 57, 24, 58, 59, 60, 61]). Furthermore, there is evidence that it is beneficial to use a linear feedback controller as a nominal stabilizing controller, which is then extended to further treat nonlinear effects (see, e.g., Refs. [62, 63, 64, 65]).

In this work, we consider the problem of computing an optimal feedback control law for a linear incompressible flow problem on a bounded domain. The spatial discretization of flow problems often leads to a very large system of equations. Standard

algorithms to compute the feedback control gain are only feasible for small systems of equations. Much recent research has focused on solving the resulting large-scale matrix equations (see, e.g., Ref. [66] and the references therein), however there are still many difficulties and open questions. First, approximating discretization matrices needed for existing numerical algorithms can be difficult (if not impossible) to extract from existing simulation code. Also, the incompressibility condition requires special numerical methods. Little is known about how such methods affect the convergence of existing control gain algorithms as the computational mesh is refined. Furthermore, there is no known method to adaptively refine the mesh to ensure accuracy.

An alternate approach to computing feedback control laws for distributed parameter systems is to first reduce the model and then solve the resulting low order matrix equation to construct the feedback gain. Proper orthogonal decomposition is a model reduction procedure that has been used for this purpose (see, e.g., [62, 67, 68, 69, 70, 65]), however there are no known guarantees of accuracy or convergence for feedback gain computations.

We investigate the use of a snapshot algorithm proposed in Ref. [14] to approximate the feedback gain operator for a linear flow problem. The algorithm is related to snapshot-based balanced model reduction methods proposed by Wilcox and Peraire [71] and Rowley [72] for finite dimensional systems. The main computational cost of the algorithm is computing solution snapshots of linear unsteady flow problems. These computations can be performed with existing software and one can also take advantage of existing techniques such as special discretization schemes, domain decomposition methods, adaptive mesh refinement, and parallel algorithms. Also, since the algorithm is based on simulation data, we bypass the potential difficulty of extracting matrices from existing simulation code.

The snapshot algorithm is also similar in spirit to computing feedback gains for infinite dimensional control problems using the Chandrasekhar equations (see, e.g., Refs. [73, 74, 75, 76]), which are a nonlinear system of differential equations whose solution approaches the gain when integrated to steady state. In contrast, the snapshot algorithm considered here computes the gain using a sequence of *linear* differential equations arising from the Lyapunov equations in the Newton-Kleinman iteration for the relevant operator Riccati equation. As discussed in Ref. [77], it can be difficult to compute the gain accurately when integrating the Chandrasekhar equations to steady state; therefore, we expect that the snapshot algorithm discussed here may be preferable for many problems. We note however that the Chandrasekhar equations have been used to compute feedback gains for linear flow problems (see, e.g., Ref. [73]); also, they can be used to provide a good stabilizing initial guess for the Newton-Kleinman iteration [77].

The remainder of this work proceeds as follows. We begin by describing the linear unsteady flow control problem. In Section 5.4, we discuss the snapshot algorithm to compute the feedback gain and its implementation for the flow problem. We then present numerical results in Section 5.5, and close with conclusions and avenues for future work.

5.3   Problem Description

We consider the control of an unsteady Stokes flow in a lid driven cavity with an open bottom. The equations of motion are given by

$$v_t = -\nabla p + \mu \Delta v + b\,u(t), \quad \nabla \cdot v = 0, \tag{5.1}$$

where $v = [v_1(t, x, y), v_2(t, x, y)]^T$ is the flow velocity vector, $p = p(t, x, y)$ is the pressure, $b = [b_1(x, y), b_2(x, y)]^T$ is a given control distribution function, and $u(t)$ is a scalar control input. We consider the following boundary and initial conditions

$$
\begin{aligned}
v_1 = 1, \; v_2 = 0 \quad &\text{on} \quad \Gamma_t \times (0, T], \\
v = 0 \quad &\text{on} \quad \Gamma_{l,r} \times (0, T], \\
-p\,n + \mu \frac{\partial v}{\partial n} = 0 \quad &\text{on} \quad \Gamma_b \times (0, T], \\
v(0, x, y) = v_0(x, y) \quad &\text{in} \quad \Omega,
\end{aligned}
\tag{5.2}
$$

where Ω is the unit square $[0, 1] \times [0, 1]$, and Γ_t, Γ_l, Γ_r, and Γ_b denote the top, left, right, and bottom walls of Ω. Also, n denotes the outward normal to the boundary.

The goal of the control is to bring the state $(v, \, p)$ to an equilibrium state, $(V, \, P)$, faster than would occur in the uncontrolled system. We assume the equilibrium state $(V, \, P)$ is a solution of (5.1), and we define the velocity and pressure fluctuations by $(v', \, p') = (v - V, \, p - P)$. Making this change of variables transforms the above Stokes flow system (5.1) and (5.2) to the following "fluctuation" Stokes equations

$$
v'_t = -\nabla p' + \mu \Delta v' + b\,u(t), \quad \nabla \cdot v' = 0,
\tag{5.3}
$$

with boundary and initial conditions

$$
\begin{aligned}
v' = 0 \quad &\text{on} \quad \Gamma \times (0, T], \\
-p\,n + \mu \frac{\partial v'}{\partial n} = 0 \quad &\text{on} \quad \Gamma_b \times (0, T], \\
v'(0, x, y) = v'_0(x, y) \quad &\text{in} \quad \Omega,
\end{aligned}
\tag{5.4}
$$

where Γ is the union of Γ_t, Γ_l, and Γ_r.

5.3.1 An Abstract Formulation

For the control problem and algorithm considered below, we place the above fluctuation Stokes problem in an abstract form. Our presentation follows Ref. [78], which considers the Dirichlet problem. See Ref. [21] for variational formulations of the related Navier-Stokes equations with both Dirichlet and outflow boundary conditions.

First, we define the function spaces relevant to the problem. Let $L^2(\Omega)$ be the Hilbert space of square integrable vector-valued functions over Ω with standard inner product

$$(f, g) = \int_\Omega f(x, y) \cdot g(x, y) \, dx \, dy,$$

and corresponding norm $\|f\| = (f, f)^{1/2}$. Define X to be the Hilbert space of weakly divergence free functions (with the above L^2 inner product and norm) given by

$$X = \left\{ f \in L^2(\Omega) \ : \ \nabla \cdot f = 0 \text{ in } \Omega, \ \ f \cdot n = 0 \text{ on } \Gamma \right\}.$$

Also let $H^m(\Omega)$ be the Hilbert space of functions in $L^2(\Omega)$ with m distributional derivatives that are all square integrable. Finally, let V be the Hilbert space

$$V = \left\{ f \in X \ : \ f \in H^1(\Omega), \ f = 0 \text{ on } \Gamma \right\},$$

with inner product $(f, g)_V = \sum(\nabla f_i, \nabla g_i)$ and norm $\|f\|_V = (f, f)_V^{1/2}$.

Now we place the fluctuation Stokes system (5.3) and (5.4) in a variational form. Taking the inner product of the fluctuation Stokes equations (5.3) with any vector φ in V gives

$$\frac{\partial}{\partial t}(v', \varphi) = -\mu(v', \varphi)_V + (b, \varphi)u(t).$$

This can be derived by integrating by parts as follows:

$$-(\nabla p, \varphi)+\mu(\Delta v', \varphi) = \int_{\partial\Omega}\left(-pn + \mu\frac{\partial v'}{\partial n}\right)\cdot\varphi\,dx\,dy+(p, \nabla\cdot\varphi)-\mu(v', \varphi)_V = -\mu(v', \varphi)_V.$$

The boundary integral is zero since φ is zero on Γ and due to the boundary condition on Γ_b in Eq. (5.4); the term $(p, \nabla\cdot\varphi)$ must also be zero since φ is in V and therefore must be divergence free.

Define the operator $A : D(A) \subset X \to X$ as follows:

$$Af = g \quad \text{if} \quad (g, \varphi) = -\mu(f, \varphi)_V \quad \text{for all } \varphi \in V.$$

Here, the set $D(A)$ consists of all functions f in V so that Af is in X. Roughly, for $f \in D(A)$, Af is the projection of $\mu\Delta f$ onto X, and functions in $D(A)$ are twice differentiable, divergence free, and satisfy the boundary conditions of the fluctuations Stokes problem. The control input operator $B : \mathbb{R} \to X$ is defined by

$$[Bu](x, y) = b(x, y)u.$$

With these operators, the above fluctuation Stokes system (5.3) and (5.4) can be written abstractly as the following differential equation over the Hilbert space X:

$$\dot{w}(t) = Aw(t) + Bu(t), \quad w(0) = w_0, \tag{5.5}$$

where $w(t) = v'(t, \cdot, \cdot)$ is a function in X for each t.

5.3.2   The Control Problem

Now we consider a specific control objective, namely to find $u \in L^2(0, \infty)$ that minimizes the cost function

$$J = \int_0^\infty [Dw]^2(t) + u^2(t) \, dt, \tag{5.6}$$

where $w(t)$ satisfies the abstract fluctuation Stokes system (5.5). Here, the controlled output operator $D : X \to \mathbb{R}$ is defined by $Dw = (w, d)$, where d is a state weighting vector in X.

Under certain assumptions, the solution to the above linear quadratic regulation (LQR) problem is given by the feedback control law

$$u(t) = -K \, w(t), \quad K = B^* \Pi, \tag{5.7}$$

where $\Pi : X \to X$ is the minimal, nonnegative definite, self-adjoint solution of the algebraic Riccati equation

$$A^* \Pi + \Pi A - \Pi B B^* \Pi + D^* D = 0. \tag{5.8}$$

Here, the asterisk (*) denotes the Hilbert adjoint operator.

In this work, we focus on computing the feedback gain operator $K : X \to \mathbb{R}$.

5.4   Computational Approach

We now describe the snapshot algorithm to compute feedback gains for infinite dimensional systems. We provide a description of the snapshot algorithm in a general infinite dimensional setting and then provide implementation details for the current problem.

5.4.1   A Snapshot Algorithm for Feedback Gains

Consider the approximation of the feedback gain operator $K = B^*\Pi$, where $\Pi : X \to X$ is the solution of the algebraic Riccati equation (5.8). We consider the following general framework. Let X be a Hilbert space with real-valued inner product $(\cdot, \cdot)$ and corresponding norm $\|x\| = (x, x)^{1/2}$. Assume the operator $A : D(A) \subset X \to X$ generates a C_0-semigroup, and the control input operator $B : \mathbb{R}^m \to X$, and the controlled output operator $D : X \to \mathbb{R}^p$ are both bounded and finite rank.

The assumptions on B and D imply that the operators must take the form

$$Bu = \sum_{j=1}^{m} u_j b_j, \quad Dx = [\,(x, d_1), \ldots, (x, d_p)\,]^T,$$

for some vectors $b_1, \ldots, b_m$ and $d_1, \ldots, d_p$ in X (see [79, Theorem 6.1]). For simplicity we focus on the case of a single input and single output, i.e., $m = 1$ and $p = 1$; the algorithms are easily modified for $m > 1$ and $p > 1$. As with most large-scale algorithms for feedback control gain computations, the snapshot algorithms require m and p to be relatively small.

For the case $m = 1$, we have $Bu = bu$ where b is a vector in X. This assumption implies that the feedback operator $K : X \to \mathbb{R}$ given by $K = B^*\Pi$ has the representation $Kx = (x, k)$, where $k = \Pi b$ is a vector in X known as a functional gain. This representation holds since $B^*x = (x, b)$ and therefore $Kx = B^*\Pi x = (\Pi x, b) = (x, \Pi b)$, since Π is self-adjoint. Below, we concentrate on approximating this functional gain.

We first apply a Newton-Kleinman iteration as modified by Banks and Ito [77] to obtain a sequence of Lyapunov equations. The solutions to the Lyapunov equations are then approximated using a snapshot algorithm. The details are as follows.

Modified Newton-Kleinman iteration [77] for the algebraic Riccati equation (5.8)

1. Chose an initial guess K_0 so that $A - BK_0$ generates an exponentially stable C_0-semigroup.

2. Compute $K_1 = B^*S_0$, where S_0 solves the Lyapunov equation

$$(A - BK_0)^*S_0 + S_0(A - BK_0) + K_0^*K_0 + C^*C = 0.$$

3. For $i = 1$ until convergence, compute $K_{i+1} = K_i - B^*S_i$, where S_i solves the Lyapunov equation

$$(A - BK_i)^*S_i + S_i(A - BK_i) + E_i^*E_i = 0, \tag{5.9}$$

and $E_i = K_i - K_{i-1}$.

This algorithm is a reformulation of the standard Newton-Kleinman iteration, which is known to converge with a quadratic rate for the class of infinite dimensional problems considered here [80].

In the above modified Newton-Kleinman iterations, we need to compute $K_1 = B^*S_0$ and $K_{i+1} = K_i - B^*S_i$ for $i \geq 1$. In the same manner as above, these operators can be represented as follows: $K_i x = (x, k_i)$, where $k_1 = S_0 b$ and $k_{i+1} = k_i - S_i b$ for $i \geq 1$. Therefore, in each iteration we do not need to compute the entire Lyapunov solution S_i, we only need the product $S_i b$. We compute this product using a snapshot algorithm below.

Consider a general infinite dimensional Lyapunov equation

$$A^*S + SA + C^*C = 0, \tag{5.10}$$

where we assume $C : X \to \mathbb{R}$ is given by $Cx = (x, c)$ with $c \in X$. It is well known

that the solution $S : X \to X$ is given by

$$Sx = \int_0^\infty e^{A^*t} C^* C e^{At} x \, dt.$$

Using the above representation of C, it can be shown [81, 14] that the solution may also be represented by

$$Sx = \int_0^\infty (x, z(t)) z(t) \, dt, \tag{5.11}$$

where $z(t) = e^{A^*t} c$ is the solution of the infinite dimensional linear differential equation

$$\dot{z}(t) = A^* z(t), \quad z(0) = c. \tag{5.12}$$

This representation leads to the following snapshot algorithm.

Snapshot algorithm [13, 14] to approximate Sx, where S solves the Lyapunov equation (5.10)

1. Compute an approximation $z^N(t)$ of the solution $z(t)$ of the differential equation (5.12).

2. Replace $z(t)$ with $z^N(t)$ in the integral representation of Sx in (5.11) and approximate the integral (by quadrature or some other method).

In Ref. [14] it is shown that if $\int_0^\infty \|z^N(t) - z(t)\|^2 \, dt \to 0$, then the resulting approximation converges to Sx .

The approximate solution $z^N(t)$ of the differential equation (5.12) need not be stored to approximate Sx. Instead, a time stepping method can be used to approximate the differential equation and the approximation to the integral can be updated while simultaneously integrating the differential equation. For example, using a piecewise linear approximation to $z(t)$ in time leads to the trapezoid rule to time step the

differential equation and the following approximation to the integral.

Trapezoid snapshot algorithm [14] to approximate Sx, where S solves the Lyapunov equation (5.10)

1. Approximate the solution of the differential equation (5.12) with the trapezoid rule:

$$(I - \Delta t A^*/2)z_{n+1} = (I + \Delta t A^*/2)z_n,$$

   where I is the identity operator.

2. Update the approximation to Sx:

$$[Sx]_{n+1} = [Sx]_n + \Delta t[(x, z_{n+1})/3 + (x, z_n)/6]z_{n+1}$$
$$+\Delta t[(x, z_{n+1})/6 + (x, z_n)/3]z_n.$$

This updating procedure can be stopped when the norm of the update to Sx (possibly unscaled by Δt) is below a certain tolerance. We note that we used a constant time step for simplicity; this is not necessary in general.

For the computations presented below, we used a "stabilized" trapezoid rule [82, 83] which starts with two backward Euler steps and continues with the standard trapezoid rule. For the two backward Euler steps, we updated Sx as follows:

$$[Sx]_1 = \Delta t(x, z_1)z_1, \qquad (I - \Delta t A^*)z_1 = c,$$
$$[Sx]_2 = [Sx]_1 + \Delta t(x, z_2)z_2, \qquad (I - \Delta t A^*)z_2 = z_1.$$

5.4.2 Implementation Details for the Stokes Control Problem

To use the above snapshot algorithm to approximate the solution of the Lyapunov equations (5.9) arising in the modified Newton iteration for the Riccati equation, we must approximate differential equations of the form

$$\dot{z}(t) = (A - BK)^* z(t), \quad z(0) = z_0.$$

We now present details on approximating the solution of this differential equation in the context of the above Stokes problem. Approximating the solution can be done using a variety of methods; here, we first discretize in time using the trapezoid rule and then discretize in space using a mixed finite element method.

For the above Stokes problem, A is the Stokes operator, B is the control input operator given by $Bu = bu$ for $b \in X$, and K is of the form $Kx = (x, k)$ for some $k \in X$. Since $A = A^*$, we have $(A - BK)^* = A - K^* B^*$, where $K^* u = ku$ and $B^* x = (x, b)$. Therefore, the above abstract differential equation is a representation of the following partial differential equation

$$z_t = -\nabla q + \mu \Delta z - k(z, b), \quad \nabla \cdot z = 0, \tag{5.13}$$

with boundary conditions

$$z = 0 \text{ on } \Gamma, \quad -qn + \mu \frac{\partial z}{\partial n} = 0 \text{ on } \Gamma_b. \tag{5.14}$$

As described above, we use the trapezoid rule for the time integration to obtain

$$\left[I - (\Delta t / 2)(A - BK)^* \right] z_n = \left[I + (\Delta t / 2)(A - BK)^* \right] z_{n-1},$$

where $z_n \approx z(t_n)$. This can be rewritten as

$$(A_s - B_s K_s) z_n = [I + (\Delta t/2)(A - BK)^*] z_{n-1},$$

where $A_s = I - (\Delta t/2)A^*$, $B_s = -(\Delta t/2)K_i^*$, and $K_s = B^*$. Then

$$z_n = (A_s - B_s K_s)^{-1} g, \quad g = [I + (\Delta t/2)(A - BK)^*] z_{n-1}.$$

To compute this inverse, we formally apply the Sherman-Morrison-Woodbury formula (see, e.g., Ref. [84]):

$$(A_s - B_s K_s)^{-1} g = (I + A_s^{-1} B_s (I - K_s A_s^{-1} B_s)^{-1} K_s) A_s^{-1} g.$$

Since $B^* x = (x, b)$ and $K^* u = ku$, the above inverse can be computed once we approximate $A_s^{-1} g$ and $A_s^{-1} k$. Thus, we need to solve the problems $A_s y_i = f_i$, for $i = 1, 2$, where $f_1 = g$ and $f_2 = k$. In the context of the above Stokes problem, these abstract steady problems take the form

$$y_i - \frac{\Delta t}{2}\big(-\nabla p_i + \mu \Delta y_i \big) = f_i, \quad \nabla \cdot y_i = 0, \tag{5.15}$$

with boundary conditions

$$y_i = 0 \text{ on } \Gamma, \quad -p_i n + \mu \frac{\partial y_i}{\partial n} = 0 \text{ on } \Gamma_b, \tag{5.16}$$

where $f_2 = k$, and $f_1 = g$ is given by

$$f_1 = g = [I + (\Delta t/2)(A - K^* B^*)] z_{n-1} = z_{n-1} + \frac{\Delta t}{2}\big(-\nabla q_{n-1} + \mu \Delta z_{n-1} - k(z_{n-1}, b) \big). \tag{5.17}$$

Here, $q_{n-1} \approx q(t_{n-1})$ and $q = q(t, x, y)$ is the pressure in the above PDE (5.13) and (6.13).

For the spatial discretization of the above steady problems, we used a mixed formulation. The approximate pressures will be constructed in the Hilbert space $X_0 = L^2(\Omega)$ of scalar-valued square integrable functions. The approximate velocities will be in the Hilbert space of vector-valued functions V_0 defined by

$$V_0 = \left\{ f \in H^1(\Omega) \, : \, f = 0 \text{ on } \Gamma \right\}.$$

Note that unlike the function space V considered in Section 5.3.1, the vector-valued functions in the space V_0 are not required to be weakly divergence free.

The above steady problem (5.15) and (5.16) can be formulated weakly as follows: Find $y_i \in V_0$ and $p_i \in X_0$ such that

$$(y_i, \phi) - \frac{\Delta t}{2} \big((p_i, \nabla \cdot \psi) - \mu(y_i, \phi)_V \big) = (f_i, \psi), \quad (\nabla \cdot y_i, \chi) = 0,$$

for all $\psi \in V_0$ and all $\chi \in X_0$. Here, $(\cdot, \cdot)$ denotes the scalar-valued or vector-valued L^2 inner product, and $(\cdot, \cdot)_V$ denotes the V inner product defined in Section 5.3.1. Also, recall $f_2 = k$, and for $f_1 = g$ we reformulate (f_1, ψ) weakly using Eq. (5.17) as follows:

$$(z_{n-1}, \psi) + \frac{\Delta t}{2} \big((q_{n-1}, \nabla \cdot \psi) - \mu(z_{n-1}, \psi)_V - (k, \psi)(z_{n-1}, b) \big).$$

The above variational problems were discretized with the Taylor-Hood finite element pair. This finite element pair satisfies the inf-sup condition, is second order accurate in the velocity variables, and is first order accurate in the pressure variables.

5.5   Numerical Results

For the numerical experiments of the Stokes flow problem we set $\mu = 1$ and applied control to the bottom half of the domain in the horizontal velocity component by taking

$$b_1(x, y) = \begin{cases} 100, & \text{for } y \leq 0.5 \\ 0, & \text{otherwise} \end{cases}, \quad \text{and} \quad b_2(x, y) \equiv 0.$$

In the performance index, the state weight function d was also applied to the bottom half of the domain:

$$d_1(x, y) = d_2(x, y) = \begin{cases} 5, & \text{for } y \leq 0.5, \\ 0, & \text{otherwise}. \end{cases}$$

All computations were performed in FreeFem++, a free two-dimensional finite element package available online [22]. The cavity domain was discretized with a uniform triangulation containing 32 elements in each coordinate direction. This corresponds to 4225 and 1089 nodes in the velocity and pressure grids for a total of 9539 degrees of freedom. We set the time step size to $\Delta t = 10^{-4}$. The tolerance for convergence of the modified Newton-Kleinman algorithm and the snapshot Lyapunov solution were both set to 10^{-4}. For the initial Newton iteration, we chose initial guess $K_0 = 0$.

Six Newton iterations were required for convergence of the functional gain. The number of time steps required for the corresponding snapshot Lyapunov solution is listed in Table 5.1.

Figures 5.1 and 5.2 contain contour plots of the functional gain for the horizontal and vertical velocity components, respectively. We demonstrated the convergence of the functional gain by repeating the above experiment on a grid of 64 elements in each coordinate direction (for a total of 37507 degrees of freedom) with a time step

Table 5.1: Lyapunov iteration number and time steps for convergence of corresponding Lyapunov solutions

Lyap. Iter.	Time Steps
1	1426
2	302
3	368
4	279
5	33
6	2

of 10^{-5}. The resulting functional gain changed on the order of 10^{-2} by measure of the global relative norm.
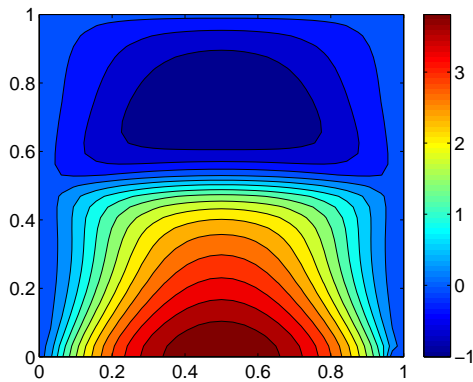
Figure 5.1: Functional gain for horizontal velocity, k_1
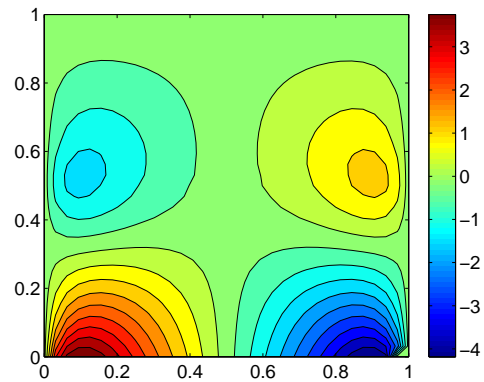
Figure 5.2: Functional gain for vertical velocity, k_2

We note that the small time step was likely required due to the nonsmooth nature of the functions b and d. An adaptive time stepping algorithm may be advantageous to use for these computations. This will be considered in future work. Also, numerical experiments on a less complex partial differential equation control problem showed that the computational speed could be improved with a good initial guess K_0 to the Newton-Kleinman iteration [85]. One can use the result of one Newton iteration as the initial guess in another Newton iteration with a finer spatial grid (see, e.g., Ref.

[86]) or time step for the snapshot algorithm. Also, as mentioned in the introduction, the Chandrasekhar equations can also be used to provide an initial guess.

5.6   Summary

We determined the feedback control gain operator for a linear incompressible flow problem using a snapshot Lyapunov equation solver in conjunction with a modified Newton-Kleinman iteration for the operator Riccati equation. The main computational cost of this approach was the numerical approximation of solutions of linear unsteady flow problems. With a sufficiently refined grid and time step, the algorithm produced a converged functional gain for the linear flow problem.

This preliminary work was intended as a proof-of-principle for computing control operators for linear flow problems without using matrix approximations of the infinite dimensional operators. In future work we will consider the performance of the closed loop system. Preliminary numerical experiments show that, as expected, the solution of the closed loop system is regulated to the equilibrium flow faster than the uncontrolled system. Other remaining problems are to consider control inputs on the boundary, include sensor measurements, and develop robust low order feedback controllers for the linearized Navier-Stokes equations.

Addendum: Observer Design for an Unsteady Stokes-Type Flow using Bioinspired Hair Sensor Arrays

In this addendum, the quasi-steady hair sensor model of Chapter 4 is combined with the control design methods of Chapter 5. The problem studied here is to build a linear quadratic Gaussian observer for an unsteady fluctuation Stokes-type flow over a square block in a channel (Figure 6.1). The observer design objective is to estimate the fluctuation Stokes velocity field in square region shown in Figure 6.1 from wall measurements provided by the horizontally and vertically mounted hair sensor arrays.
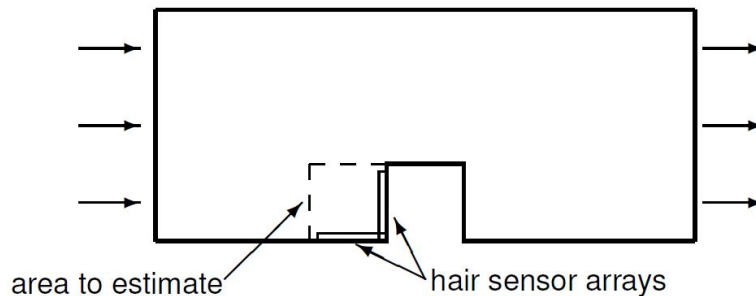
Figure 6.1: Illustration of the flow observer problem with hair sensor arrays

Recall that the linear quadratic optimal control problem presented in Chapter 5 is to find the control signal $u \in L^2(0, \infty)$ that minimizes the cost function

$$J = \int_0^\infty [Dw]^2(t) + u^2(t) \, dt, \qquad (5.6)$$

where $w(t)$, the fluctuation velocity field, satisfies the abstract fluctuation Stokes system

$$\dot{w}(t) = Aw(t) + Bu(t), \quad w(0) = w_0. \qquad (5.5)$$

Here, the controlled output operator $D : X \to \mathbb{R}$ is defined by $Dw = (w, d)$, where d

is a state weighting vector in X.

Under certain assumptions, the solution to the above LQR problem is given by the feedback control law

$$u(t) = -K\, w(t), \quad K = B^*\Pi, \tag{5.7}$$

where $\Pi : X \to X$ is the minimal, nonnegative definite, self-adjoint solution of the algebraic Riccati equation

$$A^*\Pi + \Pi A - \Pi B B^*\Pi + D^*D = 0, \tag{5.8}$$

and the asterisk (*) denotes the Hilbert adjoint operator.

The LQG problem solved here is *dual* to the above LQR problem. The problem is to estimate the state $w(t)$ (or a portion thereof) of the uncontrolled fluctuation Stokes system

$$\dot{w}(t) = Aw(t), \quad w(0) = w_0, \tag{6.1}$$

where the state is available only through indirect measurements

$$y(t) = C\, w(t) \tag{6.2}$$

and the measurement operator $C : X \to \mathbb{R}^m$ is defined by

$$C\, w(t) = [(w(t), c_1), \ldots, (w(t), c_m)]$$

where each $c_i \in X$, $i = 1, \ldots, m$, is a measurement function to be determined from the sensor models for state measurement.

The observer equations are given by

$$\dot{\hat{w}}(t) = A\hat{w}(t) + G\,(y - \hat{y}), \quad \hat{w}(0) = \hat{w}_0, \tag{6.3}$$

where $\hat{w}(t)$ is an estimate of the system state $w(t)$ and

$$\hat{y}(t) = C\,\hat{w}(t). \tag{6.4}$$

The state estimate $\hat{w}(t)$ is to be driven to the true state $w(t)$ through the observer gain $G : \mathbb{R}^m \to X$ that has the form

$$G\,y = \sum_{j=1}^{m} g_j\, y_j$$

where $y \in \mathbb{R}^m$ and each $g_j \in X$, $j = 1, \ldots, m$ is called an observer functional gain.

Under certain assumptions, the operator gain is determined as

$$G = P\,C^* \tag{6.5}$$

where $P : X \to X$ is the solution to the dual Riccati equation

$$A\,P + P\,A^* - P\,C^*\,C\,P + E\,E^* = 0, \tag{6.6}$$

and E is a weighting operator. We take $E : \mathbb{R}^m \to X$ as

$$E\,a = \sum_{i=1}^{m} e_i\, a_i.$$

where, $a \in \mathbb{R}^m$ and each $e_i \in X$, for $i = 1, \ldots, m$, is a user-specified function that weights where it is important to account for disturbances in the state estimate.

6.1 Computational Approach

We now apply the snapshot algorithm used in the previous feedback functional gain computations (Chapter 5) to the observer design problem described above. The following presentation follows Section 5.4 of Chapter 5 with dual operators and functions used in place of the control problem.

6.1.1 The Snapshot Algorithm for Observer Functional Gains

Consider the approximation of the observer gain operator $G = P C^*$, where $P : X \to X$ is the solution of the dual algebraic Riccati equation (6.6). We consider the following general framework. Let X be a Hilbert space with real-valued inner product $(\cdot, \cdot)$ and corresponding norm $\|x\| = (x, x)^{1/2}$. Assume the operator $A : D(A) \subset X \to X$ generates a C_0-semigroup, and the measurement operator $C : X \to \mathbb{R}^m$, and the observed output operator $E : X \to \mathbb{R}^p$ are both bounded and finite rank.

The assumptions on C and E imply that the operators must take the form

$$C x = [\, (x, c_1), \ldots, (x, c_m) \,]^T, \quad E a = \sum_{j=1}^{p} e_j a_j$$

for some vectors $c_1, \ldots, c_m$ and $e_1, \ldots, e_p$ in X (see [79, Theorem 6.1]).

For the case $m = 2$, we have $C x = [(x, c_1), (x, c_2)]$ where c_1 and c_2 are vectors in X. This assumption implies that the observer operator $G : \mathbb{R}^2 \to X$ given by $G = P C^*$ has the representation $G y = g_1 y_1 + g_2 y_2$, where $g_i = P c_i$ for $i = 1, 2$ are vectors in X known as observer functional gains. This representation holds since $C x = [(x, c_1), (x, c_2)]$ and therefore $G^* x = C P x = [(P x, c_1), (P x, c_2)] = [(x, P c_1), (x, P c_2)]$, since P is self-adjoint. Below, we concentrate on approximating the observer functional gains.

We first apply the Newton-Kleinman iteration as modified by Banks and Ito [77] to obtain a sequence of Lyapunov equations. The solutions to the Lyapunov equations are then approximated using a snapshot algorithm. The details are as follows.

Modified Newton-Kleinman iteration [77] for the dual algebraic Riccati equation (6.6)

1. Choose initial guesses $\{g_j^0\}_{j=1}^m$ so that $(A - G^0 C)$ generates an exponentially stable C_0-semigroup.

2. Compute $g_j^1 = P^0 c_j$ for $j = 1, \ldots, m$ where P^0 solves the Lyapunov equation

$$(A - G^0 C) P^0 + P^0 (A - G^0 C)^* + G^0 G^{0*} + E E^* = 0.$$

3. For $k = 1$ until convergence of $\{g_j^k\}_{j=1}^m$, compute $g_j^{k+1} = g_j^k - P^k c_j$, where P^k solves the Lyapunov equation

$$(A - G^k C) P^k + P^k (A - G^k C)^* + (G^k - G^{k-1}) (G^k - G^{k-1})^* = 0. \qquad (6.7)$$

This algorithm is a reformulation of the standard Newton-Kleinman iteration, which is known to converge with a quadratic rate for the class of infinite dimensional problems considered here [80].

As shown in Section 5.4 of Chapter 5, at each iteration of the above modified Newton-Kleinman iteration, the entire Lyapunov solution P^k is not required. Instead, it can be shown that the *jth* observer functional gain g_j is updated with the product $P^k c_j$ for $j = 1, \ldots, m$. We compute this product with the application of snapshot algorithm applied in Chapter 5 to the operator Lyapunov equation below.

Consider the general infinite dimensional Lyapunov equation

$$A S + S A^* + E E^* = 0, \tag{6.8}$$

where we assume $E : \mathbb{R}^m \to X$ is given by

$$E a = \sum_{i=1}^{m} e_i \, a_i$$

with each $e_i \in X$ and $a \in \mathbb{R}^m$. It is well known that the solution $P : X \to X$ is given by the observability grammian

$$P x = \int_0^\infty e^{At} E E^* e^{A^* t} x \, dt.$$

Using the above representation of E, it can be shown [13, 14] that the solution may also be represented by

$$P x = \int_0^\infty \sum_{j=1}^{m} (x, z_j(t)) z_j(t) \, dt, \tag{6.9}$$

where $z_j(t) = e^{At} c_j$ is the solution of the infinite dimensional linear differential equation

$$\dot{z}_j(t) = A z_j(t), \quad z_j(0) = e_j. \tag{6.10}$$

This representation leads to the following snapshot algorithm.

Snapshot algorithm [13, 14] to approximate $P x$, where P solves the Lyapunov equation (6.8)

1. Compute an approximation $z_j^N(t)$ of the solution $z_j(t)$ for $j = 1, \ldots, m$ of the differential equation (6.10).

2. Replace $z_j(t)$ with $z_j^N(t)$ for $j = 1, \ldots, m$ in the integral representation of $P x$

in (6.9) and approximate the integral (by quadrature or some other method).

In Ref. [14] it is shown that if

$$\sum_{j=1}^{m} \int_{0}^{\infty} \|z_j^N(t) - z_j(t)\|^2 \, dt \to 0,$$

then the resulting approximation converges to $P\,x$.

The approximate solution $z_j^N(t)$ for $j = 1, \ldots, m$ of the differential equation (6.10) need not be stored to approximate $P\,x$. Instead, a time stepping method can be used to approximate the differential equation and the approximation to the integral can be updated while simultaneously integrating the differential equation. For example, using a piecewise linear approximation to $z_j(t)$ in time leads to the trapezoid rule to time step the differential equation and the following approximation to the integral.

Trapezoid snapshot algorithm [14] to approximate $P\,x$, where P solves the Lyapunov equation (6.8)

1. Approximate the solution of the differential equation (5.12) with the trapezoid rule:

$$(I - \Delta t A^*/2)z_j^{n+1} = (I + \Delta t A/2)z_j^{n}, \quad \text{for} \quad j = 1, \ldots, m$$

where I is the identity operator.

2. Update the approximation to $P\,x$:

$$[P\,x]^{n+1} = [P\,x]^{n} + \sum_{j=1}^{m}\{\Delta t[(x, z_j^{n+1})/3 + (x, z_j^{n})/6]z_j^{n+1}$$
$$+\Delta t[(x, z_j^{n+1})/6 + (x, z_j^{n})/3]z_j^{n}\}.$$

This updating procedure can be stopped when the norm of the update to $P\,x$ is below a certain tolerance. Here, we used the following inequality to test convergence of the

Lyapunov solution

$$\frac{1}{\Delta t} \left\| [P\,x]^{n+1} - [P\,x]^n \right\|_X \leq \text{Lyapunov Tolerance.} \tag{6.11}$$

Note that although a constant time step was used to compute the Lyapunov solution this is not necessary in general.

For the computations presented below, we used a "stabilized" trapezoid rule [82, 83] which starts with two backward Euler steps and continues with the standard trapezoid rule. For the two backward Euler steps, we updated $P\,x$ as follows:

$$[P\,x]^1 = \sum_{j=1}^{m} \Delta t(x, z_j^1) z_j^1, \qquad (I - \Delta t A) z_j^1 = e_j,$$

$$[P\,x]^2 = [P\,x]^1 + \sum_{j=1}^{m} \Delta t(x, z_j^2) z_j^2, \qquad (I - \Delta t A) z_j^2 = z_j^1.$$

6.1.2 Implementation Details for the Stokes Observer Problem

To use the above snapshot algorithm to approximate the solution of the Lyapunov equations (6.7) arising in the modified Newton iteration for the dual Riccati equation, we must approximate differential equations of the form

$$\dot{z}_j(t) = (A - GC)z_j(t), \quad z_j(0) = z_j^0, \quad \text{for} \quad j = 1, \ldots, m.$$

We now present details on approximating the solution of this differential equation in the context of the Stokes problem. Approximating the solution can be done using a variety of methods; here, we first discretize in time using the trapezoid rule and then discretize in space using a mixed finite element method.

For the above Stokes problem, A is the Stokes operator, C is the measurement

operator given by $Cx = [(x, c_1), (x, c_2)]$ for c_1 and $c_2 \in X$, and G is of the form $Gy = g_1\,y_1 + g_2\,y_2$ for g_1 and $g_2 \in X$. Therefore, the above abstract differential equation 6.3 is a representation of the following partial differential equation

$$z_{j\,t} = -\nabla q + \mu \Delta z_j - g_1(z_j, c_1) - g_2(z_j, c_2), \quad \nabla \cdot z_j = 0, \tag{6.12}$$

with boundary conditions

$$z_j = 0 \text{ on } \Gamma, \quad -qn + \mu \frac{\partial z_j}{\partial n} = 0 \text{ on } \Gamma_b. \tag{6.13}$$

for $j = 1, \ldots, m$. The jth equation above (6.12) was discretized in time with the trapezoidal rule and then rewritten using the Sherman-Morrison-Woodbury identity (see, e.g., Ref. [84]), as detailed in Section 5.4.2 of Chapter 5. For each j, this leads to the numerical solution of two sparse Stokes-type systems of the form (5.15). Each Stokes system was discretized with the Taylor-Hood finite element pair. This finite element pair satisfies the inf-sup condition, is second order accurate in the velocity variables, and is first order accurate in the pressure variables.

6.2   Numerical Results

For the numerical experiments of the Stokes flow problem we set $\mu = 1$ and attempt to estimate the fluctuation flow velocity components in the square region left of the block, denoted in Figure 6.2 as R_1 and R_2.

As in Chapter 5, Section 5.3 we use the fluctuation form of the Stokes equation so that the observer is designed to estimate the fluctuations from the steady flow state.
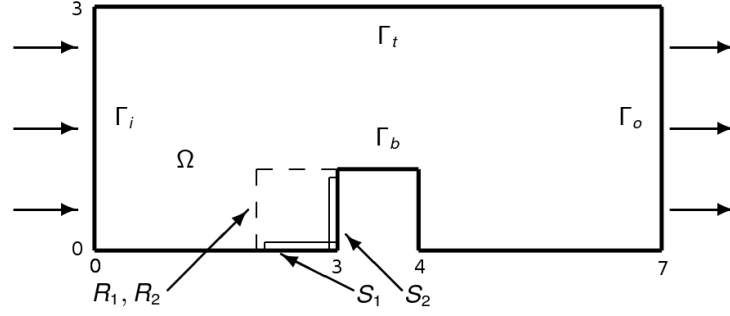
Figure 6.2: Flow observer problem schematic showing estimation regions and sensor arrays

Recall the fluctuation Stokes equations,

$$v'_t = -\nabla p' + \mu \Delta v', \quad \nabla \cdot v' = 0, \tag{6.14}$$

with boundary and initial conditions of the channel domain (Figure 6.2)

$$
\begin{aligned}
v' &= 0 &&\text{on} &&\Gamma \times (0, T], \\
-p\,n + \mu \frac{\partial v'}{\partial n} &= 0 &&\text{on} &&\Gamma_o \times (0, T], \\
v'(0, x, y) &= v'_0(x, y) &&\text{in} &&\Omega,
\end{aligned}
\tag{6.15}
$$

where Γ is the union of Γ_t, Γ_b, and Γ_i.

The estimation of the fluctuation velocity field is based of measurements from hair sensors mounted normal to the no-slip surface with uniform lengths occupying the regions labeled S_1 and S_2. The values of the observer weight functions are

$$
e_{11} = \begin{cases} 500 & (x,y) \in R_1 \\ 0 & \text{otherwise} \end{cases}
\quad e_{12} = 0 \quad \text{and} \quad e_{21} = 0, \quad
e_{22} = \begin{cases} 500 & (x,y) \in R_2 \\ 0 & \text{otherwise} \end{cases}
$$

where e_{ij} corresponds to the ith measurement of the jth vector component of the

fluctuation velocity. These observation weights correspond to the measurement of horizontal and vertical velocity fluctuations by respective arrays of horizontally and vertically mounted hair sensors.

We now determine the vector valued measurement functions c_i, $i = 1, \ldots, 2$ using the quasi-steady hair sensor models. Recall the quasi-steady hair sensor models for moment $M(t)$ and shear force $F(t)$ developed in Chapter 4, Section 4.3,

$$M(t) = \int_0^\ell \frac{1}{2} C_d(\text{Re}_\xi)\, \rho\, d(\xi)\, u(t, \xi)^2\, \xi\, d\xi \tag{4.7}$$

and

$$F(t) = \int_0^\ell \frac{1}{2} C_d(\text{Re}_\xi)\, \rho\, d(\xi)\, u(t, \xi)^2\, d\xi. \tag{4.8}$$

where C_d is a local drag coefficient computed as

$$\log C_d \approx -\frac{2}{3} \log \text{Re}_\xi + \frac{5}{2}, \tag{4.6}$$

Re_ξ is the local Reynolds number,

$$\text{Re}_\xi = \frac{u(t, \xi)\, d(\xi)}{\nu},$$

$u(t, \xi)$ is the flow velocity incident on the longitudinal axis of the hair, $d(\xi)$ is the hair diameter, ν is the fluid kinematic viscosity, ρ is the fluid density, and ℓ is the hair length. The substitution of (4.6) into (4.7) and (4.8) leads to the following relationships for moment and shear

$$M(t) = p \int_0^\ell u(t, \xi)^{4/3} \xi d\xi \tag{6.16}$$

and

$$F(t) = p \int_0^\ell u(t, \xi)^{4/3} d\xi \tag{6.17}$$

where $p = 6.07 \, \rho \, d^{1/3} \, \nu^{2/3}$ is a constant factored from the integrand of (4.7) and (4.8), assuming a uniform hair diameter.

Here, we base the measurement for the Stokes observer design on the moment equation (6.16). For consistency with the linear measurement operator, $C : X \to \mathbb{R}^m$, the hair output is linearized by approximating $u(t, \xi)^{4/3}$ with $u(t, \xi)$. For simplicity, a single output is determined for each sensor array by integrating the moment equation (6.16) over the direction tangential to the wall. This leads to the measurement equations

$$y = C \, v' = \left[\int_\Omega c_1 \cdot v' \, d\mathbf{x}, \int_\Omega c_2 \cdot v' \, d\mathbf{x} \right] \tag{6.18}$$

where c_1 and c_2 are vectors with components

$$c_{11} = \begin{cases} 10 \, y & (x, y) \in S_1 \\ 0 & \text{otherwise} \end{cases}, \quad c_{12} = 0$$

and

$$c_{21} = 0, \quad c_{22} = \begin{cases} 10 \, (3 - x) & (x, y) \in S_2 \\ 0 & \text{otherwise} \end{cases}$$

where c_{ij} denotes the *ith* measurement and *jth* vector component and the factor of 10 was chosen arbitrarily.

All computations were performed in FreeFem++, a free two-dimensional finite element package available online [22]. The cavity domain was discretized with an unstructured triangulation containing 10225 and 2617 nodes in the velocity and pressure grids for a total of 23067 degrees of freedom. We set the time step size to $\Delta t = 10^{-4}$. The tolerance for convergence of the modified Newton-Kleinman algorithm and the

snapshot Lyapunov solution were both set to 10^{-3}. For the initial Newton iteration, we chose initial iterates of $g_1 = g_2 = 0$.

Six Newton iterations were required for convergence of the functional gain. The number of time steps required for the corresponding snapshot Lyapunov solution is listed in Table 6.1.

Table 6.1: Lyapunov iteration number and time steps for convergence of corresponding Lyapunov solutions

Lyap. Iter.	Time Steps
1	14360
2	10244
3	10080
4	7499
5	1806
6	2

Figures 6.3 and 6.4 contain plots of the observer functional gains for the horizontal and vertical velocity components of the horizontally mounted hair sensor array, respectively. The nonzero values shown in Figures (6.3) and (6.4) show that the
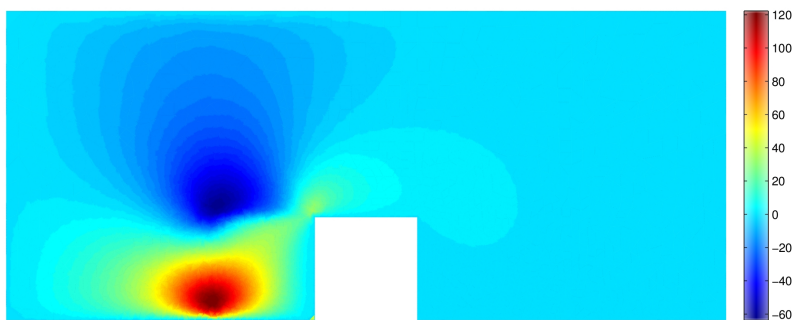
Figure 6.3: Observer functional gain for horizontal velocity measurement of horizontally mounted hair sensor array, g_{11}

observer gains contribute to the state estimate through regions to the left of the block. In both plots, the scalar fields shown are similar to *horizontal* velocity fields
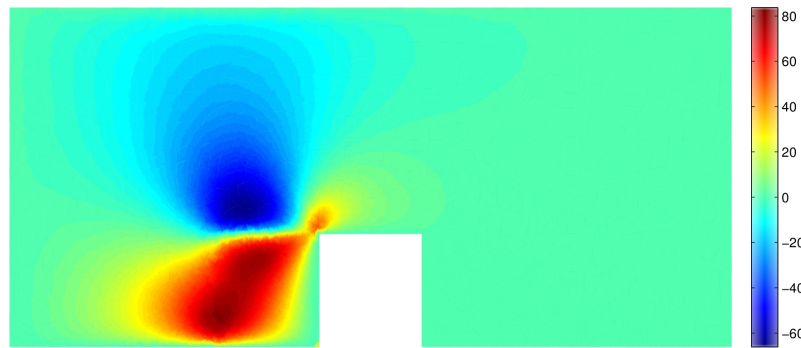
Figure 6.4: Observer functional gain for vertical velocity measurement of horizontally mounted hair sensor array, g_{12}

of a counterclockwise rotating vortex in front of the block. Since both observer gains correspond to the horizontally mounted sensor array, it appears that the observer gains reflect the detection of the horizontal velocity component. This observation is consistent with the function of the hair sensors mounted on the horizontal wall since they are also activated by the horizontal component of velocity.

Figures 6.5 and 6.6 contain plots of the observer functional gains for the horizontal and vertical velocity components of the vertically mounted hair sensor array, respectively. The nonzero values shown in Figures (6.5) and (6.6) also show that
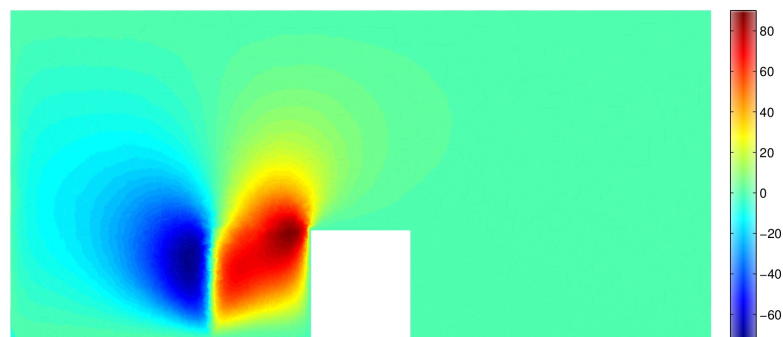
Figure 6.5: Observer functional gain for horizontal velocity measurement of horizontally mounted hair sensor array, g_{21}
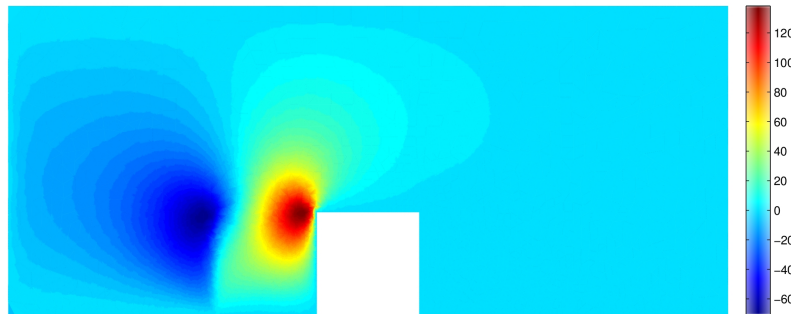
Figure 6.6: Observer functional gain for vertical velocity measurement of horizontally mounted hair sensor array, g_{22}

the observer gains contribute to the state estimate through regions to the left of the block. Here, the observer gains are similar to *vertical* velocity fields of a counterclockwise rotating vortex in front of the block and correspond to the vertically mounted hair sensor array. Since the vertically mounted sensor array is forced by the vertical component of velocity, it appears that the observer gains reflect the detection of the vertical velocity component. This is also consistent with the function of hair sensors mounted on a vertical wall as they are forced by the vertical component of velocity.

With the computation of the observer functional gains, the observer design is complete. We now test the effectiveness of the Stokes flow observer design to estimate the velocity fields in the square region in front of the block. Recall the abstract form of the fluctuation Stokes observer system,

$$\dot{w}(t) = Aw(t), \quad w(0) = w_0, \tag{5.5}$$

$$y(t) = C\,w(t), \tag{6.2}$$

$$\dot{\hat{w}}(t) = A\hat{w}(t) + G\,(y - \hat{y}), \quad \hat{w}(0) = \hat{w}_0, \tag{6.3}$$

$$\hat{y}(t) = C\,\hat{w}(t). \tag{6.4}$$

The error between actual state $w(t)$ and state estimate $\hat{w}(t)$ may be computed as $\tilde{w}(t) = w(t) - \hat{w}(t)$, so that $\dot{\tilde{w}}(t) = \dot{w}(t) - \dot{\hat{w}}(t)$. Then, subtracting (5.5) from (6.3) leads to a set of error equations

$$\dot{\tilde{w}}(t) = (A - GC)\tilde{w}, \quad \tilde{w}(0) = \tilde{w}_0 \tag{6.19}$$

where $\tilde{w}_0$ is an initial state estimate error.

Note that the fluctuation Stokes problem is exponentially stable. That is, there exists constants $M \geq 1$ and $\omega > 0$, so that $\|w(t)\| \leq M\,e^{-\omega t}\,\|w(0)\|$. As a result, for any initial state estimate error, sensor feedback in the observer equation (6.3) is not necessary for state estimation in the steady state. For the fluctuation Stokes for system, the performance of the Stokes observer design must be evaluated as the system comes to equilibrium. To this end, we compared the performance of the observer without sensor feedback

$$\dot{\hat{w}}(t) = A\hat{w}(t), \quad \hat{w}(0) = \hat{w}_0,$$

to that with sensor feedback using the observer gain (6.3) for a common initial error.

Figures (6.7) and (6.8) contain plots of the L^2-norm of the flow state estimate error $\tilde{w}$ in R_1 and R_2 (see Figure 6.2) for an initial error, $\tilde{w}_0 = [-U, -V]$, where U and V are the time-independent mean velocity fields of the Stokes flow problem over a block. Using LQG designed observer functional gains, the flow feedback provided by the hair sensor arrays is shown to significantly contribute to the estimation of the flow velocity field. In this first attempt at flow estimation we anticipate that estimator performance may be further improved by tuning the LQR design parameters and by including multiple measurements within each sensor array.
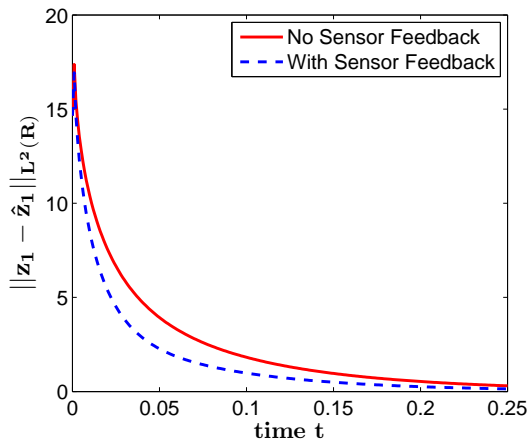
Figure 6.7: Evolution of state estimate error of horizontal velocity in R_1 with and without hair sensors
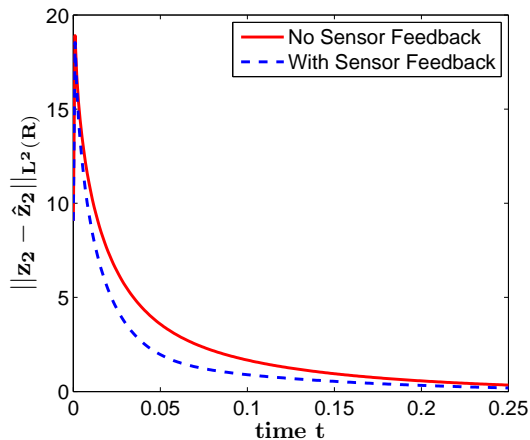
Figure 6.8: Evolution of state estimate error of vertical velocity in R_2 with and without hair sensors

6.2.1   Summary

In this addendum, the snapshot Lyapunov solver (explored in the flow control design in Chapter 5) was applied to a linear quadratic Gaussian (LQG) observer design for a Stokes-type flow over a block in a channel. Here, flow measurement was accomplished with a horizontally and vertically mounted patch of hair sensors, where a single measurement was computed for each array based on the quasi-steady hair sensor model developed in Chapter 4. The resulting observer functional gains reflected the velocity components detected by each hair sensor array. In conjunction with the LQG design, the flow feedback provided by the hair sensors was shown to significantly contribute to the estimation of the flow velocity field away from the wall. These results support the application of artificial hair sensors in flow control designs. In addition, these results exhibit the utility of the snapshot Lyapunov solver for linear quadratic control design. Future work should test the efficacy of linear and extended LQG flow observer designs for the estimation of unsteady and spatially developing flows at higher Reynolds numbers.

Acknowledgments

8 Conclusions

Many animals use hair-like receptors that are activated by fluid flows for prey detection and tracking or enhancing locomotion. For flow control applications where aero- or hydrodynamic forces play a critical role in the dynamics of a body, artificial hair sensors (AHS) are one means of flow detection for the feedback of flow information related to the fluid forces. The collection of papers in this thesis investigated the detection of aero- and hydrodynamically important fluid flows with hair-like structures.

A distributed parameter model of a hair coupled to flow data was developed and simulated in unsteady flow separation using the finite element method. Observations of a single hair response to the flow showed that the moment at the base of the hair provided a time accurate indication of the incident flow velocity and direction, including flow reversal due to separation. A parameter investigation showed surface forces from the external airflow dominated the inertial forces of the hair. Observations between the output of the hair sensor array and the flow simulation showed that the hair-cell array detected both the onset and span of reversed flow, the location of the point of zero wall shear stress, the movement of eddies away from the wall, and the formation of a small counter-rotating pair of eddies upstream of the larger clockwise eddy. For this research, future work should include validation of the hair sensor models proposed here. Although physical experimentation may be the best approach to validation, high fidelity simulation of the fluid-structure interaction between the hair and flow could also be used.

By considering disparate time scales between the hair dynamics and air flow environment, a quasi-steady model relating the boundary layer shape to the resultant moment and shear force at the base of the hair was developed. The hair model was nondimensionalized using momentum thickness as a length scale and the resultant

moment and shear force at the base of the hair (output) was computed in Falkner-Skan boundary layer flow. Based on the hair output, distinct lengths of maximum hair output sensitivity (optimal lengths) were determined. Hair length was also shown to be a critical design parameter, as both hair shapes experienced a sharp decay in output sensitivity as length moved away from the optimal values. However, the linearly tapered hair showed slightly less penalty in output sensitivity for suboptimal lengths. On an order of magnitude basis, the range of optimal hair lengths was in exact agreement with the range of measured hair receptor lengths on bat wings ($\sim 100 - 1000\,\mu m$). This result supports the hypothesis that bats use hair receptors for boundary layer detection and give length guidelines for artificial hair sensor design and application. The optimization of hair shape in boundary layer flows is a topic of current research.

Having developed an understanding of the hair sensor behavior in fluid flows, linear quadratic control methodologies for observer designs were developed in Chapter 5. Here, we determined the feedback control gain operator for a linear incompressible flow problem using a snapshot Lyapunov equation solver in conjunction with a modified Newton-Kleinman iteration for the operator Riccati equation. The main computational cost of this approach was the numerical approximation of solutions of linear unsteady flow problems. With a sufficiently refined grid and time step, the algorithm produced a converged functional gain for the linear flow problem. This approach was then extended to an infinite dimensional observer design for an unsteady Stokes-type flow with hair sensor arrays. Two patches of surface mounted hair sensor arrays were shown to effectively contribute to the estimation of the flow field away from the wall. This result supports the use of hair sensors for flow field measurement and estimation. Additionally, these results exhibit the utility of the snapshot Lyapunov solver for linear quadratic control design of distributed parameter systems.

Here, our future work will see the use of adaptive time-stepping algorithms and adaptive grid refinement with the snapshot Lyapunov solver to study their effect on the convergence of feedback and observer functional gains.

Bibliography

[1] G. Crowley and L. Hall. Histological observations on the wing of the grey-headed flying-fox (Pteropus-Poliocephalus) (Chiroptera, Pteropodidae). *Aust. J. Zool.*, 42:215–231, 1994.

[2] J.M. Zook. The neuroethology of touch in bats: cutaneous receptors of the wing. In *Neurosci. Abstr. 78.21*, 2005.

[3] S Sterbing-D'Angelo, M Chadha, and C Moss. Representation of the wing membrane in somatosensory cortex of the bat, *Eptesicus fuscus*. In *Neurosci. Abstr. 370.4*, 2008.

[4] S. Coombs. Smart skins: information processing by lateral line flow sensors. *Auton. Robot.*, 11:255–261, 2001.

[5] S. Coombs, J. G. New, and M. Nelson. Information-processing demands in electrosensory and mechanosensory lateral line systems. *J. Physiology-Paris*, 96:341–354, 2002.

[6] C. Magal, O. Dangles, P. Caparroy, and J. Casas. Hair canopy of cricket sensory system tuned to predator signals. *J. Theor. Biol.*, 241:459–466, 2006.

[7] O. Dangles, D. Pierre, C. Magal, F. Vannier, and J. Casas. Ontogeny of air-motion sensing in cricket. *J. Exp. Biol.*, 209:4363–4370, 2006.

[8] F.G. Barth and A. Höller. Dynamics of arthropod filiform hairs. V. The response of spider trichobotheria to natural stimuli. *Phil. Trans. R. Soc. Lond. B*, 354:183–192, 1999.

[9] F.G. Barth. How to catch the wind: Spider hairs specialized for sensing the movement of air. *Naturwissenschaften*, 87:51–58, 2000.

[10] W. Shyy, Y. Lian, J. Tang, D. Viieru, and H. Liu. *Aerodynamics of Low Reynolds Number Flyers*. Cambridge University Press, 2008.

[11] B. Dickinson, J. Singler, and B. Batten. The detection of unsteady flow separation with bioinspired hair cell sensors. In *Proceedings of the 26th AIAA Aerodynamic Measurement Technology and Ground Testing Conference*, 2008. AIAA 2008-3937.

[12] B.T. Dickinson, J.R. Singler, and B.A. Batten. Mathematical modeling of biologically inspired hair receptor arrays in laminar unsteady flow separation. Submitted to Journal of Fluids and Structures.

[13] J.R. Singler. Approximate low rank solutions of Lyapunov equations via proper orthogonal decomposition. In *Proceedings of the 2008 American Control Conference*, pages 267–272, 2008.

[14] J.R. Singler. Convergent snapshot algorithms for infinite dimensional Lyapunov equations. submitted for publication.

[15] J.T. Albert, O.C. Freiedrich, H.E. Denchant, and F.G. Barth. Arthropod touch reception: spider hair sensilla as rapid touch receptors. *J. Comp. Physiol. A*, 187:303–312, 2001.

[16] J. Engel, J. Chen, D. Bullen, and C. Liu. Polyurethane rubber as MEMS material: characterization and demonstration of an all polymer two-axis artificial haircell flow sensor. In *18th IEEE International Conference on Micro Electro Mechanical Systems*, pages 279–282, 2005.

[17] J. Engel, J. Chen, C. Liu, and D. Bullen. Polyurethane rubber all-polymer artificial hair cell sensor. *J. MEMS*, 15:729–736, 2006.

[18] Y. Yang, N. Chen, C. Tucker, J. Engel, S. Pandya, and C. Liu. From artificial hair cell sensor to artificial lateral line system: development and application. In *20th IEEE International Conference on Micro Electro Mechanical Systems*, pages 577–580, 2007.

[19] B.T. Dickinson, J.R. Singler, and B.A. Batten. Modeling of bioinspired sensors for flow separation detection for micro air vehicles. In *3rd AIAA Flow Control Conference*, 2006. AIAA 2006-3019.

[20] P. Gresho and R. Sani. *Incompressible flow and the finite element method - advection-diffusion and isothermal laminar flow*. John Wiley and Sons, 1998.

[21] J. Heywood, R. Rannacher, and S. Turek. Artificial boundaries and flus and pressure conditions for the incompressible Navier-Stokes equations. *Int. J. Numer. Meth. Fluids*, 22:325–352, 1996.

[22] F. Hecht, O. Pironneau, A. Le Hyaric, and K. Ohtsuka. *Freefem++ Version 2.23-2*. http://www.freefem.org/ff++.

[23] J. Gere. *Mechanics of Materials*. Brooks/Cole, 2001.

[24] J. Kim. Control of turbulent boundary layers. *Phys. of Fluids*, 15:1093–1105, 2003.

[25] G. von Békésy. Shearing microphonics produced by vibrations near the inner and outer hair cells. *J. Acoust. Soc. Am.*, 25:786–790, 1953.

[26] O. Dangles, C. Magal, D. Pierre, A. Oliver, and J Casas. Variation in morphology and performance of predator-sensing system in wild cricket populations. *J. Exp. Biol.*, 208:461–468, 2005.

[27] J. Zook. *Evolution of Nervous Systems*, volume 3, chapter Evolution of Nervous Systems Vol 3, pages 215–226. Academic Press: Oxford, 2006.

[28] W. Shyy, M. Berg, and D. Ljungqvist. Flapping and flexible wings for biological and micro vehicles. *Prog. Aerosp. Sci.*, 35:455–506, 1999.

[29] P.B.S. Lissaman. Low-reynolds-number airfoils. *Ann. Rev. Fluid Mech.*, 15:223–239, 1983.

[30] T.J. Mueller and J.D. DeLaurier. Aerodynamics of small vehicles. *Ann. Rev. Fluid Mech.*, 35:89–111, 2005.

[31] Y. Ozaki, T. Ohyama T. Yasuda, and I. Shimoyama. An airflow sensor modeled on wind receptor hairs of insects. In *The 13th International Conference on Micro-Electro-Mechanical Systems*, pages 531–536, 2000.

[32] M. Dijkstra, J.J. van Baar, R.J. Wiegerink, T.S.J. Lammerink, J.H. de Boer, and G.J.M. Krijnen. Artificial sensory hairs based on the flow sensisitve receptor hairs of crickets. *J. Micromechs. Mircoeng.*, 15:S132–S138, 2005.

[33] G.J. Schmitz, Ch Brüker, and P Jacobs. Manufacture of high-aspect-ratio micro-hair sensor arrays. *J. Micromech. Microeng.*, 15:1904–1910, 2005.

[34] M. Billone and S. Raynor. Transmission of radial shear forces to cochlear hair cells. *J. Acoust. Soc. Am.*, 54:1143–1156, 1973.

[35] J.-H. Nam, J.R. Cotton, and J.W. Grant. Effect of fluid forcing on vestibular hair bundles. *J. Vestib. Res.*, 15:263–278, 2005.

[36] A.P. Patterson and J.W. Hardin. Flight speeds of five species of vespertilionid bats. *J. Mammal.*, 50:152–153, 1969.

[37] A.J. Aranyosi and D.M. Freeman. Sound-induced motions of individual cochlear hair bundles. *Biophys. J.*, 87:3536–3546, 2004.

[38] H. Schlichting and K. Gersten. *Boundary Layer Theory*. Springer, 2000.

[39] J. Davis. *Dynamics of Continuous Media*. Macmillan, 1987.

[40] O. Zienkiewicz, R. Taylor, and P. Nithiarasu. *The Finite Element Method for Fluid Dynamics*. Elsevier Butterworth-Heinemann, 2005.

[41] W.R. Sears and D.P. Telionis. Boundary-layer separation in unsteady flow. *SIAM J. Appl. Math*, 28:215–235, 1975.

[42] T. Cebeci. The laminar boundary layer on a circular cylinder stated impulsively from rest. *J. Comput. Phys.*, 31:153–172, 1979.

[43] M. Högberg, M. Chevalier, and D.S. Henningson. Linear compensator control of a pointsource induced perturbation in a Falkner-Skan-Cooke boundary layer. *Phys. Fluids*, 15:2449–2452, 2003.

[44] M. Chevalier, J.Hœpffner, E. Åkervik, and D.S. Henningson. Linear feedback control and estimation applied to instabilities in spatially developing boundary layers. *J. Fluid Mech.*, 588:163–187, 2007.

[45] M. Feughelman. *Mechanical Properties and Structure of Alpha-Keratin Fibres.* University of New South Wales Press, 1997.

[46] R.L. Panton. *Incompressible Flow.* Wiley, 2005.

[47] H.B. Keller and T. Cebeci. Accurate numerical methods for boundary layer flows. I: Two dimensional laminar flows. In *Lecture Notes in Physics: Proc. Int. Conf. Numer. Meth. Fluid Dyn., 2nd, Berkley, Calif. Springer-Verlag*, pages 92–100, 1971.

[48] R.E. Carpenter. Flight physiology of flying foxes, Pteropus poliocephalus. *J. Exp. Biol.*, 114:619–647, 1985.

[49] S.M. Swartz, M B. Bennett, and D.R. Carrier. Wing bone stresses in free flying bats and the evolution of skeletal design for flight. *Nature*, 359:726–729, 1992.

[50] J.B. Akins, M.L. Kennedy, G.D. Schnell, C.Sánchez-Hernández, M. Romero-Almaraz, M.C. Wooten, and T.L. Best. Flight speeds of three species of neotropical bats: Glossophaga soricina, Natalus stramineus, and Carollia subrufa. *Acta Chiropterol.*, 9:477–482, 2007.

[51] U.M. Norberg. Allometry of bat wings and legs and comparison with bird wings. *Philosophical Transactions of the Royal Society of London. Series B, Biological Sciences*, 292:359–398, 1981.

[52] M. Drela. An analysis and design system for low Reynolds number airfoils. In *Proceedings of the Conference on Low Reynolds Number Aerodynamics*, pages 1–12, 1989.

[53] V. Barbu, I. Lasiecka, and R. Triggiani. Tangential Boundary Stabilization of Navier-Stokes Equations. *Mem. Amer. Math. Soc.*, 181(852), 2006.

[54] J.A. Burns and J.R. Singler. Feedback control of low dimensional models of transition to turbulence. In *Proceedings of the 44th IEEE Conference on Decision and Control and European Control Conference*, pages 3140 – 3145, 2005.

[55] J.A. Burns and J.R. Singler. Modeling transition: New scenarios, system sensitivity and feedback control. In *Transition and Turbulence Control*, pages 1–37. World Scientific, 2006.

[56] L. Cortelezzi and J.L. Speyer. Robust reduced-order controller of laminar boundary layer transitions. *Phys. Rev. E*, 58(2-A):1906 – 1910, 1998.

[57] M. Högberg, T.R. Bewley, and D.S. Henningson. Linear feedback control and estimation of transition in plane channel flow. *J. Fluid Mech.*, 481:149–175, 2003.

[58] J. Kim and T. R. Bewley. A linear systems approach to flow control. In *Ann. Rev. Fluid Mech. Vol. 39*, pages 383–417. Annual Reviews, Palo Alto, CA, 2007.

[59] K.H. Lee, L. Cortelezzi, J. Kim, and J. Speyer. Application of reduced-order controller to turbulent flows for drag reduction. *Phys. Fluids*, 13(5):1321 – 1330, 2001.

[60] A.C. Or, L. Cortelezzi, and J.L. Speyer. Robust feedback control of Rayleigh-Benard convection. *J. Fluid Mech.*, 437:175 – 202, 2001.

[61] J.-P. Raymond. Feedback boundary stabilization of the two-dimensional Navier-Stokes equations. *SIAM J. Control Optim.*, 45(3):790–828, 2006.

[62] J.A. Atwell, J.T. Borggaard, and B.B. King. Reduced order controllers for Burgers' equation with a nonlinear observer. *Int. J. Appl. Math. Comput. Sci.*, 11(6):1311–1330, 2001.

[63] J.A. Burns and B.B. King. A reduced basis approach to the design of low-order feedback controllers for nonlinear continuous systems. *J. Vib. Control*, 4(3):297–323, 1998.

[64] J.A. Burns, B.B. King, and D. Rubio. Feedback control of a thermal fluid using state estimation. *Int. J. Comput. Fluid Dyn.*, 11(1-2):93–112, 1998.

[65] C.H. Lee and H.T. Tran. Reduced-order-based feedback control of the Kuramoto-Sivashinsky equation. *J. Comput. Appl. Math.*, 173(1):1–19, 2005.

[66] V. Simoncini. A new iterative method for solving large-scale Lyapunov matrix equations. *SIAM J. Sci. Comput.*, 29(3):1268–1288, 2007.

[67] J.A. Atwell and B.B. King. Proper orthogonal decomposition for reduced basis feedback controllers for parabolic equations. *Math. Comput. Modelling*, 33(1-3):1–19, 2001.

[68] J.A. Atwell and B.B. King. Reduced order controllers for spatially distributed systems via proper orthogonal decomposition. *SIAM J. Sci. Comput.*, 26(1):128–151, 2004.

[69] H.T. Banks, Ricardo C.H. del Rosario, and R.C. Smith. Reduced-order model feedback control design: numerical implementation in a thin shell model. *IEEE Trans. Automat. Control*, 45(7):1312–1324, 2000.

[70] G.M. Kepler, H.T. Tran, and H.T. Banks. Reduced order model compensator control of species transport in a CVD reactor. *Optim. Contr. App. Met.*, 21(4):143–160, 2000.

[71] K. Willcox and J. Peraire. Balanced model reduction via the proper orthogonal decomposition. *AIAA J.*, 40(11):2323–2330, 2002.

[72] C. W. Rowley. Model reduction for fluids, using balanced proper orthogonal decomposition. *Internat. J. Bifur. Chaos Appl. Sci. Engrg.*, 15(3):997–1013, 2005.

[73] J. Borggaard, J. Burns, and L. Zietsman. Computational challenges in control of partial differential equations. In *Proceedings of the 2nd AIAA Flow Control Conference*, 2004. AIAA 2004-2526.

[74] J.A. Burns and K.P. Hulsing. Numerical methods for approximating functional gains in LQR boundary control problems. *Math. Comput. Modelling*, 33(1-3):89–100, 2001.

[75] K. Ito and R.K. Powers. Chandrasekhar equations for infinite-dimensional systems. *SIAM J. Control Optim.*, 25(3):596–611, 1987.

[76] K. Ito and R.K. Powers. Chandrasekhar equations for infinite-dimensional systems. II. Unbounded input and output case. *J. Differ. Equations*, 75(2):371–402, 1988.

[77] H.T. Banks and K. Ito. A numerical algorithm for optimal feedback gains in high-dimensional linear quadratic regulator problems. *SIAM J. Control Optim.*, 29(3):499–515, 1991.

[78] K. Ito and F. Kappel. The Trotter-Kato theorem and approximation of PDEs. *Math. Comp.*, 67(221):21–44, 1998.

[79] J. Weidmann. *Linear Operators in Hilbert Spaces*. Springer-Verlag, New York, 1980.

[80] J.A. Burns, E.W. Sachs, and L. Zietsman. Mesh independence of Kleinman–Newton iterations for Riccati equations in Hilbert space. *SIAM J. Control Optim.*, 47(5):2663–2692, 2008.

[81] J.R. Singler. Transition to turbulence, small disturbances, and sensitivity analysis. I. A motivating problem. *J. Math. Anal. Appl.*, 337(2):1425–1441, 2008.

[82] R. Rannacher. Finite element solution of diffusion problems with irregular data. *Numer. Math.*, 43(2):309–327, 1984.

[83] A. Hansbo. Nonsmooth data error estimates for damped single step methods for parabolic equations in Banach space. *Calcolo*, 36(2):75–101, 1999.

[84] G. H. Golub and C.F. Van Loan. *Matrix Computations.* Johns Hopkins University Press, Baltimore, MD, 1996.

[85] J.R. Singler and B.A. Batten. A comparison of balanced truncation methods for closed loop systems. In *Proceedings of the American Control Conference*, pages 820–825, 2009.

[86] K. Morris and C. Navasca. Solution of algebraic Riccati equations arising in control of partial differential equations. In *Control and Boundary Analysis*, pages 257–280. Chapman & Hall/CRC, Boca Raton, FL, 2005.